Published in final edited form as:

Immunity. 2022 August 09; 55(8): 1483–1500.e9. doi:10.1016/j.immuni.2022.07.001.

Lung fibroblasts facilitate pre-metastatic niche formation by remodeling the local immune microenvironment

Zheng Gong[1,4], **Qing Li**[1,4], **Jiayuan Shi**[1], **Jian Wei**[1], **Peishan Li**[1], **Chih-Hao Chang**[1,2,3], **Leonard D. Shultz**[1], **Guangwen Ren**[1,2,3,5,*]

[1]The Jackson Laboratory, Bar Harbor, ME 04609, USA

[2]Tufts University School of Medicine, Boston, MA 02111, USA

[3]Graduate School of Biomedical Sciences and Engineering, University of Maine, Orono, ME 04469, USA

[4]These authors contributed equally

[5]Lead contact

SUMMARY

Primary tumors are drivers of pre-metastatic niche formation, but the coordination by the secondary organ toward metastatic dissemination is underappreciated. Here, by single-cell RNA-sequencing and immunofluorescence, we identified a population of cyclooxygenase 2 (COX-2)-expressing adventitial fibroblasts that remodeled the lung immune microenvironment. At steady-state, fibroblasts in the lungs produced prostaglandin E2 (PGE2), which drove dysfunctional dendritic cells (DCs) and suppressive monocytes. This lung-intrinsic stromal program was propagated by tumor-associated inflammation, particularly the pro-inflammatory cytokine interleukin-1β, supporting a pre-metastatic niche. Genetic ablation of *Ptgs2* (encoding COX-2) in fibroblasts was sufficient to reverse the immune-suppressive phenotypes of lung-resident myeloid cells, resulting in heightened immune activation and diminished lung metastasis in multiple breast cancer models. Moreover, the anti-metastatic activities of DC-based vaccine and PD-1 blockade were improved by fibroblast-specific *Ptgs2* deletion or dual inhibition of PGE2 receptors EP2 and EP4. Collectively, lung-resident fibroblasts reshape the local immune landscape to facilitate breast cancer metastasis.

Graphical Abstract

*Correspondence: Gary.Ren@jax.org.

Author contributions

G.R., Z.G. and Q.L. conceived the project, designed the study and performed the data analysis. Z.G. and Q.L. performed the *in vivo* and *in vitro* studies, statistical analysis and generated the figures. J.S. and P.L. helped with *in vitro* experiments. C.C. and J.W. helped with bone marrow chimera assay. L.D.S. provided critical assistance on experimental design. G.R., Z.G. and Q.L. interpreted the data and wrote the manuscript.

Declaration of interests

The authors declare no competing of interests.

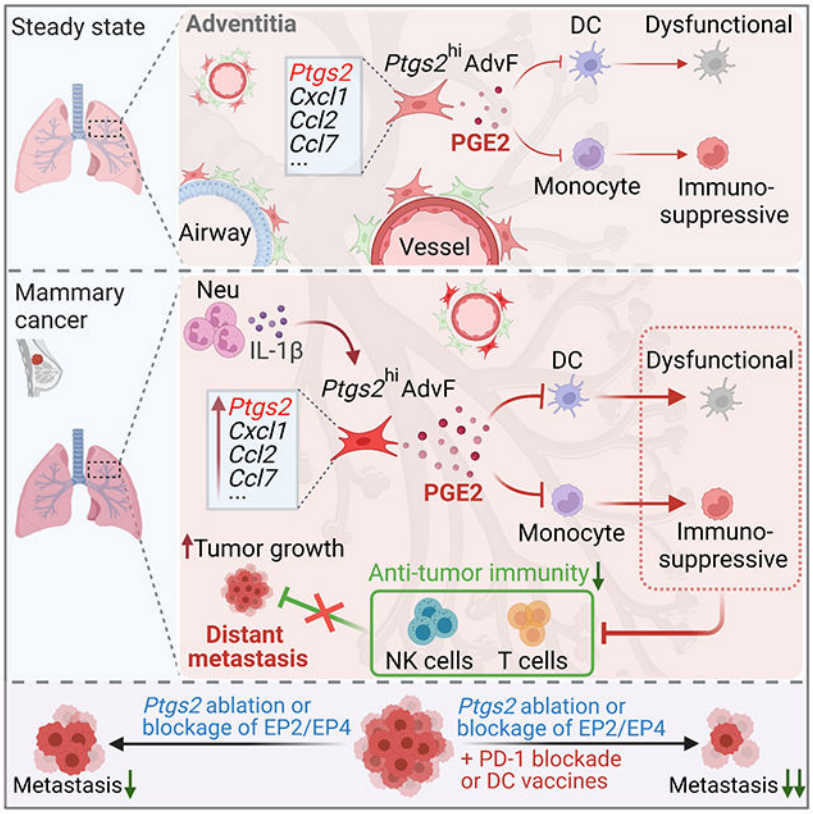

INTRODUCTION

Solid cancer metastasis, which remains the major cause of cancer-related death, is a complex process consisting of a series of steps from primary tumor invasion and intravasation, to tumor cell survival in the circulation, to extravasation and distant organ colonization (Lambert et al., 2017). Among these steps, organ colonization is regarded as a rate-limiting step for metastasis due to robust tissue defenses against disseminated tumor cells (DTCs) (Massague and Obenauf, 2016). Successful colonization is only achieved when organ environments coordinate with newly arrived DTCs to engage immune-inhibitory machinery that surpasses the organ's defensive barriers. A deep understanding of the mechanisms within the organ environment that regulate DTC rejection or acceptance is essential for uncovering the fundamental biology of metastasis and for developing therapeutics against metastasis.

Organ environments and cancer genomic heterogeneity are two primary determinants of metastatic organotropism, a key characteristic of metastasis denoting that the spread of cancer occurs in a non-random manner with certain tumor types inclined to metastasize to specific organs (Gao et al., 2019). Relative to our increasing knowledge of the cancer-intrinsic genes mediating cancer cells' organotropic metastases, characterization of the metastasis-supporting organ microenvironments, especially the stroma, is lacking. Many fundamental questions remain unanswered, including whether the susceptibility of organs to tumor metastasis is intrinsic to the organ or induced by primary tumors or involves an

interplay of both, and what are the key organ-resident components dictating successful DTC colonization. Answering these questions will help unveil the basis of metastatic organotropism and accelerate design of organ-specific targeting strategies in the clinical management of metastases.

The lung is one of the most common sites of metastasis, frequently colonized in various late-stage solid cancers. Formation of the lung pre-metastatic niche, which is initiated by factors secreted from primary tumors, is a key preparation stage prior to the arrival of DTCs (Liu and Cao, 2016; Peinado et al., 2017). Bone marrow (BM)-derived immunosuppressive myeloid cells, such as neutrophils, monocytes, and macrophages, are well-characterized components of the pre-metastatic niche (Kaplan et al., 2005; Kitamura et al., 2015). These myeloid cells facilitate building a hospitable environment for future invading DTCs mainly through their suppression of local anti-tumor immunity, as well as their extravasation-promoting and trophic effects on DTCs (Altorki et al., 2019; Kitamura et al., 2015; Spiegel et al., 2016).

In contrast to the known roles of BM-derived myeloid cells, how the lung-resident stromal fibroblasts, which play decisive roles in a variety of lung diseases (Samarelli et al., 2021; Ushakumary et al., 2021), contribute to formation of the pre-metastatic and metastatic niches is less understood. Here, using single cell RNA-sequencing (scRNA-seq) and immunofluorescence-based spatial profiling, we identified a metastasis-promoting lung adventitial fibroblast population that constitutively expressed high levels of inflammatory genes, including *Ptgs2*, *Cxcl1*, *Ccl2*, *Ccl7* and *Il6*. These *Ptgs2*^{hi} fibroblasts reprogrammed various types of myeloid cells to be dysfunctional or immunosuppressive. In mouse models of breast cancer, tumor-associated inflammation enhanced this fibroblast-intrinsic modulation of myeloid cells. Genetic or pharmacological inhibition of the lung fibroblast signaling pathway involving prostaglandin E2 (PGE2) largely restored lung-resident anti-tumor immunity, reduced lung metastasis of breast cancer, and increased the efficacy of immunotherapeutics in treating lung metastasis. Collectively, our work defines a function for lung-resident stromal cells in eliciting a robust immunosuppressive niche. Targeting lung stromal factors could be an effective strategy to treat lung metastases.

Results

Lung fibroblasts endow myeloid cells with a dysfunctional or immunosuppressive phenotype via expression of cyclooxygenase 2 (COX-2)

Formation of an immune dysfunctional lung pre-metastatic niche, which is elicited by primary tumor progression, is critical for early-arrived DTCs to escape anti-tumor immunity (Liu and Cao, 2016; Peinado et al., 2017). In a mouse model of orthotopic breast cancer (4T1) (Figure S1A), we indeed found that lung-resident CD24^{+}CD11c^{+}MHC-II^{+} dendritic cells (DCs) (Headley et al., 2016; Misharin et al., 2013) (Figure S1B), the antigen presenting cells (APCs) triggering anti-tumor adaptive immunity (Vermaelen and Pauwels, 2005), had reduced capacity to stimulate T cell proliferation at the pre-metastatic stage (Figure S1C). To evaluate how the pre-metastatic lung environment modulates DCs and possibly other APCs, we employed an exogenous myeloid cell transplantation system using bone marrow-derived DCs (BM-DCs), which comprise conventional DCs and other antigen presenting myeloid

cells (Helft et al., 2015; Lutz et al., 2017). Upon intravenous (IV) injection of fluorescently labeled healthy BM-DCs into naïve and 4T1 tumor-bearing mice (pre-metastatic stage), we monitored the implanted cells in lungs and other organs and tissues for their expression of major histocompatibility complex (MHC) class I and II, the primary molecules on DCs that mediate antigen presentation to T cells (Wculek et al., 2020). Exogenous BM-DCs engrafted in lungs had the lowest levels of MHC-I and MHC-II expression compared to those in other organs and tissues examined, including peripheral blood (PB), BM, spleen and liver (Figure 1A). This occurred in both naïve and tumor-bearing mouse recipients (Figure 1A), suggesting that the lung stroma at a steady state has an intrinsic capacity to disable BM-DCs, and that this effect is further reinforced by tumor-bearing conditions.

Using *ex vivo* co-culture of BM-DCs with various types of lung tissue cells, including $CD45^+$ leukocytes, $CD31^+$ endothelial cells, $CD326^+$ epithelial cells and CD140a $(PDGFR\alpha)^+$ fibroblasts, we identified $CD140a^+$ fibroblasts as being able to inhibit MHC-I and MHC-II expression (Figure 1B) and antigen uptake ability of BM-DCs (Figure S1D). Supporting this, a close proximity of implanted BM-DCs to $CD140a^+$ cells within the lung interstitium was detected *in vivo* (Figure 1C). Despite this, direct cell-cell contact was not necessary for lung fibroblasts to modulate BM-DCs, as lung fibroblast-conditioned medium (CM) was as effective as lung fibroblast cells in modulating BM-DCs (Figures 1D and S1E). These results suggested that DC dysfunction is elicited by lung-resident fibroblasts via soluble factors.

To identify the lung fibroblast-derived soluble factor(s), we leveraged the RNA sequencing (RNA-seq) data from BM-DCs without and with treatment by lung fibroblast CM. By Ingenuity Pathway Analysis, we obtained the top upstream regulator candidates (Figure S1F) that may stimulate changes in BM-DCs. With MHC-II expression as a DC functional indicator, PGE2 was screened as the most effective factor in repressing MHC-II expression on BM-DCs (Figure 1E). PGE2, a prostaglandin playing multifaceted roles in inflammation and cancer, is generated from arachidonic acid via the actions of cyclooxygenase (COX) enzymes, COX-1 and COX-2 (Nakanishi and Rosenberg, 2013). As expected, lung fibroblasts isolated from naïve mice secreted PGE2 (Figure S1G). At the transcriptional level, lung fibroblasts expressed a higher level of *Ptgs2* (encoding COX-2) than *Ptgs1* (encoding COX-1) (Figure S1H). Furthermore, PGE2 in lung fibroblasts was almost exclusively contributed by COX-2, with no apparent compensatory activity from COX-1, as lung fibroblasts isolated from *Ptgs2* knockout (KO) mice showed minimal PGE2 production (Figure S1I). In the *ex vivo* co-culture system, *Ptgs2* ablation in lung fibroblasts largely abrogated their regulatory effects on BM-DCs (Figures 1F and S1J). Consequently, the antigen-specific $CD4^+$ and $CD8^+$ T cell hyporesponsiveness induced by lung fibroblast-exposed BM-DCs was substantially reversed by *Ptgs2* deficiency in fibroblasts (Figure 1G). Therefore, COX-2-PGE2 is essential for lung fibroblasts to endow BM-DCs with a dysfunctional phenotype.

By further probing the transcriptomic profiles of BM-DCs, we found that lung fibroblasts, in a COX-2-dependent manner, inhibited the expression of genes associated with antigen uptake, processing, and presentation in BM-DCs, and purified PGE2 acted similarly to lung fibroblasts (Figure 1H). In addition, the expression levels of multiple immunosuppression-

associated genes, including *Arg1*, *Cd274*, *Il10*, *Nos2*, *Ptgs2*, and *Pdcd1lg2*, were increased in BM-DCs upon stimulation by wild type (WT) lung fibroblasts (Figure 1H). Further analysis of the BM-DC transcriptomes precluded the possibility of lung fibroblast-mediated DC differentiation into macrophages (Figure S1K), which can be immunosuppressive (Pathria et al., 2019). Induction of these immunosuppression-associated genes in BM-DCs was primarily dependent on lung fibroblast-derived COX-2, but to a lesser extent on PGE2, as *Ptgs2*-KO in lung fibroblasts reversed the effect on most of these genes, while PGE2 alone only activated a subset (Figure 1H). We reasoned that COX-2-derived other prostaglandins than PGE2 (Funk, 2001) in lung fibroblasts may be involved in this immunosuppression-associated gene induction in BM-DCs. As a functional consequence, lung fibroblast CM-educated BM-DCs served to suppress antigen-specific T cell proliferation (Figure 1I) and the cytotoxicity of natural killer (NK) cells (Figure 1J), which are pivotal to restraining DTCs at the early colonization stage (Li et al., 2020b; Lopez-Soto et al., 2017). Again, these effects were dependent on lung fibroblast-derived COX-2 (Figures 1I and 1J). Therefore, via COX-2-PGE2 and possibly other COX-2-derived prostaglandins, lung fibroblasts endow exogenous BM-DCs with dysfunctional and immunosuppressive capacities.

Next, we asked whether this stromal-myeloid cell interaction also occurs in other myeloid lineage cells. Monocytic cells play crucial roles in a diversity of lung diseases and metastasis (Baharom et al., 2017; Qian et al., 2011), and we therefore determined whether monocytic cells are altered by lung fibroblasts. Upon stimulation with lung fibroblast CM, BM-derived monocytes (Figure S1L) increased their expression of a series of immunosuppressive genes, including *Arg1*, *Ptgs2*, *Nos2* and *Il10*, which was partially dependent on lung fibroblast-derived COX-2 (Figure 1K). Correspondingly, lung fibroblast-educated monocytes suppressed T cell proliferation (Figure 1L) and NK cell cytotoxicity (Figure S1M), in a lung fibroblast COX-2-dependent manner. In accordance with these *ex vivo* results, monocytes showed a tissue-specific gene expression pattern *in vivo*, with higher expression of immunosuppressive genes in lung-infiltrating monocytes than those isolated from BM or PB, which was more prominent under tumor-bearing conditions (Figure S1N). Taken together, lung fibroblasts, via expression of COX-2, reprogram various myeloid cell types to be dysfunctional or immunosuppressive.

Ptgs2-expressing lung fibroblasts modulate the lung-resident immune microenvironment at the steady state

To determine whether the COX-2-dependent stromal-immune interaction is specific to the lung, we employed $Ptgs2^{Luc}$ reporter mice (Ishikawa et al., 2006) to compare COX-2 signals in different organs isolated from naïve mice. Compared to other organs tested, including brain, bone (femur and tibia), intestine, stomach, heart, liver, spleen, pancreas and kidney, the lungs expressed a higher level of *Ptgs2* (Figures 2A and S2A). In human, a similarly high *PTGS2* expression in lungs was detected (Figure 2B) through analyses of human tissue microarray data (Rhodes et al., 2004). The characteristically high levels of *Ptgs2* expression and PGE2 production in the lung were mainly contributed by lung fibroblasts, shown by comparison of the major types of lung cells isolated from naïve mice (Figure 2C). Further, lung fibroblasts were superior to fibroblasts isolated from other tested tissues (bone,

heart, liver, spleen and mammary glands) in their *Ptgs2* expression and PGE2 secretion (Figure 2D) and endowed myeloid cells (monocytes) with a more potent immunosuppressive phenotype (Figure S2B). Thus, the lung is a unique organ with constitutively high *Ptgs2* (or *PTGSE2*) expression, predominantly in resident fibroblasts.

To better understand the role of the COX-2-dependent lung fibroblast program in reprogramming the lung-resident immune microenvironment, we generated fibroblast-targeted *Ptgs2* conditional KO (cKO) mice ($Ptgs2^{\Delta Fb}$). With *Ptgs2* deficiency, lung fibroblasts lost COX-2 expression and PGE2 production (Figures 2E and 2F). Upon profiling the lung immune microenvironment (Figures S1B and S2C) of naïve WT and $Ptgs2^{\Delta Fb}$ mice, we found that the total numbers of adaptive immunity-related cells, including DCs, $CD4^+$ and $CD8^+$ T cells, were increased in $Ptgs2^{\Delta Fb}$ mice (Figure 2G). In contrast, the frequencies of lung myeloid cells (alveolar macrophages, neutrophils and conventional monocytes) were comparable between cKO and WT mice, except for an increase in non-alveolar macrophages in cKO mice (Figure S2D).

Aside from these cell frequency changes, ablation of fibroblast *Ptgs2* led to increased expression of MHC-I and MHC-II on lung-resident DCs, along with their increased capacity to take up antigens (Figure 2H). Further characterization of the two primary types of lung-resident DCs, $CD103^+$ and $CD11b^+$ DCs (Desch et al., 2013; Neyt and Lambrecht, 2013), showed that fibroblast-COX-2-mediated MHC-I and MHC-II suppression occurred similarly in both DC subtypes (Figure 2I). Beyond MHC molecules, a broad spectrum of genes associated with antigen uptake, processing and presentation were increased in both $CD11b^+$ and $CD103^+$ lung-resident DCs isolated from $Ptgs2^{\Delta Fb}$ mice, compared to those from WT mice (Figures 2J and S2E). Such COX-2 loss-induced lung-resident DC changes were reversed by injection of PGE2 into $Ptgs2^{\Delta Fb}$ mice, confirming the role of COX-2-PGE2 signaling in modulation of lung-resident DCs *in vivo* (Figure S2F).

As for the lung-infiltrating conventional monocytes, their expression of a series of immunosuppressive genes, including *Arg1*, *Arg2*, *Cd274*, *Ptgs2*, *Nos2* and *Il10*, was reduced by *Ptgs2* cKO (Figures 2K and S2G). In contrast to the above transcriptional changes in myeloid cells, expression of genes encoding essential mediators of anti-tumor immunity, including T cell cytokines interferon γ (IFNγ), tumor necrosis factor α (TNFα) and interleukin 12 (IL-12), cytotoxic protein perforin-1, chemokines C-X-C motif chemokine ligand (CXCL) 9 and CXCL10, and transcriptional factors signal transducer and activator of transcription 1 (STAT1) and eomesodermin (EOMES) (Vesely et al., 2011), were elevated in $CD45^+$ immune cells isolated from $Ptgs2^{\Delta Fb}$ mouse lungs compared to WT mice (Figure S2H). In accordance with the results from bulk RNA-seq and quantitative PCR (qPCR) (Table S1), lung immune profiling by scRNA-seq showed similar changes induced in lung-resident DCs and monocytes by *Ptgs2* cKO (Figures S2I–S2L). Collectively, loss of COX-2 in $CD140a^+$ fibroblasts led to quantitative and qualitative reprogramming of the lung immune microenvironment characterized by diminished immune dysfunction and immunosuppression, together with augmented anti-tumor adaptive immunity.

Identification of the *Ptgs2*-expressing fibroblasts by scRNA-seq

To identify the specific lung fibroblast subset expressing *Ptgs2*, we performed scRNA-seq on sorted $CD45^{-}CD31^{-}CD326^{-}$ cells, which include $CD140a^{+}$ fibroblasts and other stromal cells. Unbiased clustering through Seurat identified 15 clusters. Upon removal of the contaminating cells, five major stromal cell types were classified, including $CD140a^{+}$ fibroblasts, mesothelial cells, pericytes, smooth muscle cells and myofibroblasts, based on their specific marker gene expression (Habermann et al., 2020; Xie et al., 2018; Zepp et al., 2017) (Figures S3A). Among the five types of stromal cells, *Ptgs2* was predominantly expressed in $CD140a^{+}$ fibroblast clusters, and was particularly highly enriched in cluster 1 (Figures S3B and S3C), which accounted for ~25% of all $CD140a^{+}$ fibroblasts (Figures S3B and S3D).

Analysis of other signature genes of the $Ptgs2^{hi}$ fibroblast cluster (cluster 1) revealed *Has1* as the most prominent (Figure S3C). *Has1* encodes hyaluronan synthase 1 (HAS1), which can be induced in mesenchymal lineage cells in response to inflammatory stimuli, including PGE2, and serves as a mediator of inflammation (Siiskonen et al., 2015). In a work studying human idiopathic pulmonary fibrosis, a unique human $HAS1^{hi}$ extracellular matrix (ECM)-producing lung stromal population was characterized (Habermann et al., 2020). We thus speculated that these $HAS1^{hi}$ human stromal cells correspond to $Ptgs2^{hi}$ fibroblasts in mice. Through analysis of human lung scRNA-seq data (Habermann et al., 2020) (Figure S3E), the *PTGS2*-expressing human lung stromal cells fell into the $PDGFRA^{+}$ $HAS1^{+}$ cluster (Figure S3F). Thus, scRNA-seq analyses identified a unique lung $Ptgs2^{hi}$ $CD140a^{+}$ fibroblast population in mouse and human.

As the $Ptgs2^{hi}$ cells were exclusively $CD140a^{+}$ fibroblasts, we next purified $CD140a^{+}$ lung cells using $CD140a^{EGFP}$ mice for higher-resolution scRNA-seq (Figure 3A). Within the $CD140a^{+}$ lung fibroblasts, 6 distinct clusters were revealed by unbiased clustering analysis and, among them, cluster 0 was identified as the $Ptgs2^{hi}$ fibroblasts (Figure 3B). Other genes encoding the key enzymes of the PGE2 synthesis pathway were not co-clustered with *Ptgs2* (Figure 3C). The top 10 enriched genes in this $Ptgs2^{hi}$ lung fibroblast subset were, without exception, inflammation-associated genes. In addition to *Ptgs2* and *Has1*, signature genes include *Cxcl1* (C-X-C motif chemokine ligand 1), *Il6* (interleukin 6), *Tnfaip6* (TNF alpha induced protein 6), *Mt1* (metallothionein-1), *Zfp36* (zinc finger protein 36 homolog), *Ccl7* (C-C motif chemokine ligand 7), *Ptx3* (pentraxin 3) and *Ccl2* (C-C motif chemokine ligand 2) (Figure 3D). All of them play crucial roles in different stages of inflammation and are inducible by pro-inflammatory cytokines such as interleukin 1 beta (IL-1β) (Doni et al., 2019; King et al., 2009; Mackay, 2001; Mittal et al., 2016; Samad et al., 2001; Sanduja et al., 2012; Siiskonen et al., 2015; Subramanian Vignesh and Deepe, 2017; Tanaka et al., 2014). The expression of other canonical inflammatory genes appeared independent of *Ptgs2*, as the transcriptional levels of the majority of them remained unaltered upon *Ptgs2* deletion in $CD140a^{+}$ fibroblasts (Figure 3E). Based on the gene expression profile, we surmised that the $Ptgs2^{hi}$ fibroblast subset is a pro-inflammatory signal-responsive lung stromal element that modulates local immune responses.

In line with the inflammatory gene expression, a series of inflammation-related pathways were enriched in the $Ptgs2^{hi}$ lung fibroblast subset, such as “Inflammatory response” and

"Cellular response to interleukin-1" (Figure 3F). Analysis of the transcription factor (TF) activities indicated that, compared to two other major fibroblast subsets (clusters 1 and 2, Figure 3B), the *Ptgs2*^{hi} fibroblasts possess more robust activities of TFs associated with inflammation, such as signal transducer and activator of transcription 3 (STAT3), nuclear factor kappa b subunit 1 (NFKB1), and cAMP responsive element binding protein 1 (CREB1) (Taniguchi and Karin, 2018; Wen et al., 2010; Yu et al., 2009) (Figure 3G). By analyzing human normal tissue transcriptome data (Roth et al., 2006), a large proportion of the mouse *Ptgs2*^{hi} fibroblast signature genes were found within the top listed genes co-expressed with *PTGS2*, including *IL6*, *CCL2*, *CXCL1*, *PTX3* and *TNFAIP6*, in the human lung, but not other human tissues and organs examined (Figure 3H). This co-expression profile was similarly detected in mice upon analysis of the scRNA-seq data from CD140a^{+} fibroblasts (Figure 3I). Collectively, these data suggested that the *Ptgs2*^{hi} lung fibroblast subset is an intrinsic stromal component that maintains an inflammation-prone immunoregulatory milieu in the lung at the steady state.

Ptgs2^{hi} lung fibroblasts are mainly located within the lung adventitial space

Given that *Ptgs2*^{hi} lung fibroblasts could be an inflammation-regulatory stromal population, we wondered how this subset of stromal cells spatially interacts with resident inflammatory cells of the lung. To this end, we leveraged published scRNA-seq datasets with available information on gene expression profiles associated with anatomical locations in mouse and human lungs (Travaglini et al., 2020). By mapping reported signature genes of eight anatomically annotated mouse lung stromal subsets onto our scRNA-seq data (Figure S3A), we found that naïve mouse lung CD140a^{+} fibroblasts mainly comprise three known stromal subsets -- adventitial fibroblasts (AdvF), alveolar fibroblasts (AlvF) and lipofibroblasts (LipF) (Figure 4A). In particular, the *Ptgs2*^{hi} lung fibroblasts (cluster 1, Figure 4A) were characterized as a subpopulation of the *Serpinf1*- and *Pi16*-expressing AdvFs (Figures 4B and 4C), which are fibroblasts localized around arteries, veins, and airways in the lung playing critical roles in pulmonary vascular remodeling and tissue immunity (Dahlgren and Molofsky, 2019; Stenmark et al., 2011). Similar to the mouse findings, *PTGS2*-expressing human lung stromal cells mostly fell into the AdvF subset (Figure 4D). Therefore, the *Ptgs2*^{hi} lung fibroblasts were categorized as a subpopulation of AdvF.

Using immunofluorescence, we further pinpointed the spatial localization of *Ptgs2*^{hi} fibroblasts in the lung, as well as their interactions with myeloid cells. In naïve lungs, we compared the distributions of COX-2^{+} fibroblasts within the adventitial versus alveolar regions. These cells mainly resided within the lung adventitial space (Figures 4E and 4F), consistent with the scRNA-seq analysis. Moreover, in the pre-metastatic lung, COX-2^{+} fibroblasts were physically close or adjacent to a diversity of myeloid cells, including CD11b^{+} DCs, CD103^{+} DCs and Ly6C^{+} monocytes (**Figures 4G–4J**). Based on their expression of myeloid cell chemokines (CXCL1, CCL7 and CCL2), immunomodulators (COX-2 and TNFAIP6), and ECM modulator (HAS1), we speculated that the adventitial location of COX-2^{+} fibroblasts favors recruitment and reprograming of infiltrated inflammatory cells to form an immunosuppressive pre-metastatic lung niche. Hence, *Ptgs2*^{hi} lung fibroblasts were identified as a subpopulation of AdvF that physically interact with various types of resident myeloid cells in the pre-metastatic lung.

IL-1β reinforces the phenotype of *Ptgs2*^{hi} lung fibroblasts

To define whether tumor-bearing conditions impact the COX-2-dependent lung stromal program, we employed AT3 and AT3-*gcsf* orthotopic breast tumor models that enabled us to decouple the effects of tumor versus host inflammation. The AT3 line originates from an MMTV-PyMT tumor and induces marginal host inflammation (Stewart and Abrams, 2007), whereas the AT3-*gcsf* line was constructed to overexpress granulocyte-colony stimulating factor (G-CSF) that stimulates strong host inflammation, specifically neutrophilia (Gong et al., 2022), similar to the 4T1 model used above.

At the pre-metastatic stage of the AT3 and AT3-*gcsf* orthotopic models (Figure S4A), CD140a^{+} lung fibroblasts were isolated for comparison of their *Ptgs2* expression and PGE2 production. While transcriptional and protein levels of COX-2 expression and PGE2 production in lung fibroblasts were mildly increased by AT3 tumor-bearing, they were all further induced in the AT3-*gcsf* model (Figures 5A and S4B). In addition, the total number of CD140a^{+} fibroblasts was increased in AT3-*gcsf* tumor-bearing mice (Figure S4C). Consistent with COX-2-PGE2 upregulation in lung fibroblasts, elevated host inflammation reinforced myeloid cell reprogramming (MHC-I and MHC-II expression in exogenous BM-DCs) in the pre-metastatic lung *in vivo* (Figure S4D). Therefore, host inflammation (neutrophilia) served to heighten the COX-2-dependent lung fibroblast program.

Based on the scRNA-seq result showing “Cellular response to interleukin-1” as one of the top enriched pathways in *Ptgs2*^{hi} lung fibroblasts (Figure 3F), we speculated that the pro-inflammatory cytokine IL-1 could be a relevant host inflammation-associated factor. Indeed, exogenous addition of IL-1β stimulated lung fibroblasts to highly express *Ptgs2*, as well as *Ptgs1* and *Ptges,* albeit not as strongly (Figure 5B), which was abrogated by IL-1 receptor (*Il1r1*) deficiency in lung fibroblasts (Figure 5B). This IL-1β-dependent COX-2 regulation in lung fibroblasts was further confirmed at the protein level (Figures 5C and S4E). Pharmacological inhibition of the NFκB pathway mitigated IL-1β-induced *Ptgs2* expression and PGE2 production in lung fibroblasts (Figure 5D), confirming a functional role for the high level of NFκB activity detected in *Ptgs2*^{hi} lung fibroblasts (Figures 3G and S4F). Thus, an IL-1β-IL-1R-NFκB signaling axis was revealed in the regulation of COX-2-PGE2 in lung fibroblasts.

By RNA-seq, IL-1β was found to elicit broad transcriptional changes in lung fibroblasts *ex vivo*. In addition to prostaglandin synthesis genes (Figure 5E), expression levels of the majority of *Ptgs2*^{hi} lung fibroblast signature genes, particularly *Ptgs2*, *Il6*, *Ccl7*, *Cxcl1* and *Ccl2*, were elevated in lung fibroblasts after IL-1β stimulation (Figures 5F and 5G). *In vivo*, IL-1β treatment increased the percentage of COX-2^{+} lung fibroblasts but not the total number of fibroblasts (Figures 5H, 5I, and S4G), and stimulated expression of *Ptgs2*^{hi} lung fibroblast signature genes in lung fibroblasts (Figures S4H and S4I). Moreover, host deficiency of *Il1r1* led to a reduction in the proportion of COX-2^{+} lung fibroblasts *in vivo* under steady-state, suggesting an essential role for endogenous IL-1β-IL-1R signaling in lung fibroblast modulation (Figure S4J). Human lung fibroblast-like cells similarly elevated their expression of *Ptgs2*^{hi} fibroblast signature genes (*PTGS2*, *IL6*, *CCL2*, *CCL7* and *CXCL1*) and PGE2 production upon IL-1β treatment, partially dependent on NFκB (Figure

S4K). Thus, in both mouse and human, IL-1β was revealed to be a key regulator of the lung fibroblast program.

Finally, we determined the cellular source of IL-1β. Similar to our previous finding showing potent expression of *Il1b* in lung-infiltrating neutrophils in the 4T1 model (Li et al., 2020a), lung neutrophils in the AT3 models released abundant soluble IL-1β (Figure 5J). *Ex vivo*, lung fibroblast expression of *Ptgs2*, *Il6*, *Ccl2*, *Ccl7* and *Cxcl1* was exclusively elevated upon co-culture with lung neutrophils isolated from AT3-*gcsf* tumor-bearing mice. Neutralization of IL-1β partially abolished this effect, indicating the indispensable role of neutrophil-derived IL-1β in neutrophil-lung fibroblast crosstalk (Figure 5K). Corroborating these *ex vivo* findings, a spatially close interaction was detected between COX-2^{+} lung fibroblasts and Ly6G^{+} neutrophils in the pre-metastatic lung (Figure 5L). Taken together, these data support a model whereby the myeloid cell regulatory program intrinsic to *Ptgs2*^{hi} lung AdvF can be further reinforced by neutrophil-derived IL-1β during progression of tumor-associated inflammation (Figure 5M).

Genetic ablation of *Ptgs2* in CD140a^{+} fibroblasts mitigates lung metastasis

Using the *Ptgs2*$^{\Delta Fb}$ model, we next determined the functional contribution of *Ptgs2*^{hi} lung AdvF in breast cancer lung metastasis. To define their role in the pre-metastatic niche to accommodate DTC colonization, we utilized a modified experimental lung metastasis model, in which luciferase-labeled AT3 (AT3-Luc) cells were IV injected into WT and *Ptgs2*$^{\Delta Fb}$ mice bearing orthotopic AT3 tumors (unlabeled) at their pre-metastatic stage. Two weeks later, while the primary tumors did not differ between the two mouse strains, metastatic colonization by AT3-Luc cells in *Ptgs2*$^{\Delta Fb}$ mouse lungs was 4-fold lower than in WT mice (Figure 6A). Depletion of DCs (Figure S5A) and possibly other myeloid cells using clodronate liposomes (Perruche et al., 2008; Wang et al., 2016) partially reversed this effect (Figure 6B), indicating that myeloid cells are functionally involved in *Ptgs2*^{hi} AdvF-mediated modulation of metastasis *in vivo*. Using a different syngeneic breast tumor line, E0771, this mitigation of metastatic colonization in *Ptgs2*$^{\Delta Fb}$ mice was similarly detected (Figures S5B and S5C). These results support a colonization-promoting role of *Ptgs2*^{hi} lung AdvF.

To rule out possible confounding effects of CD140a-lineage hematopoietic cells that however do not express CD140a (Miura et al., 2021) (Figures S6A and S6B), we also generated BM-chimeric mice in which WT hematopoietic cells were engrafted in lethally irradiated WT or *Ptgs2*$^{\Delta Fb}$ mice (Figures S6C and S6D). Using this BM-chimeric *Ptgs2*$^{\Delta Fb}$ model, we validated that loss of *Ptgs2* in CD140a^{+} fibroblasts led to similar changes in lung-resident immune cells (Figures S6E–K), as detected in the original *Ptgs2*$^{\Delta Fb}$ model. Accordingly, targeted deletion of *Ptgs2* in fibroblasts in the BM-chimeric model reduced lung colonization by breast tumor cells (Figure S6L).

To better recapitulate human breast cancer patients with metastases, we exploited a spontaneous lung metastasis model in which metastases were assessed 2 weeks after surgical removal of the primary tumors (Figure 6C, *left*). We observed fewer lung metastases spontaneously occurring in *Ptgs2*$^{\Delta Fb}$ mice, compared to WT mice (Figures 6C and 6D). Lastly, we evaluated the impact of fibroblast-specific *Ptgs2* deficiency on spontaneous

metastases in the genetically engineered MMTV-PyMT model by crossing the *Ptgs2*$^{\Delta Fb}$ strain with the MMTV-PyMT strain. Consistent with the transplantation models, deletion of *Ptgs2* in CD140a^{+} fibroblasts reduced spontaneous lung metastases developed in MMTV-PyMT mice (Figure 6E). In sum, the COX-2-PGE2-dependent lung fibroblast program functions to promote breast cancer metastasis to the lung.

Targeting COX-2-PGE2 signals synergizes with immunotherapeutics in controlling lung metastasis

Given the essential role of the COX-2-PGE2 pathway in lung fibroblasts in reprogramming the lung immune microenvironment and facilitating metastatic progression, we endeavored to target this pathway in preclinical models as a strategy to boost local anti-tumor immunity and thereby improve efficacy of clinically used immunotherapeutics such as DC vaccine and immune checkpoint blockade (Palucka and Banchereau, 2013; Sharma and Allison, 2015). When we first tested a selective COX-2 inhibitor, celecoxib, it was found ineffective in reducing metastatic colonization in the AT3 model (Figure S7A). As a possible explanation, celecoxib did not reduce PGE2 levels in the lungs of naïve or tumor-bearing mice (Figure S7B). We reasoned that this might be due to a compensatory effect from another COX isoform, COX-1, and therefore we speculated that blockage of PGE2 receptors may represent a more effective approach to repress PGE2 signals *in vivo*.

In lung-resident DCs and conventional monocytes, EP2 and EP4 were expressed at high levels among the four mouse PGE2 receptors (EP1-EP4) (Figure S7C). While administration of either EP2 or EP4 antagonist was ineffective in reducing AT3 tumor colonization, possibly due to compensatory effects between these two PGE2 receptors, administration of the two antagonists together showed a greater than 10-fold reduction of metastatic colonization in the modified experimental metastasis model (Figure 7A). Consistent with this potent efficacy in treating metastasis, MHC molecule expression and antigen uptake ability of lung DCs, as well as the proportion of lung-infiltrating CD4^{+} and CD8^{+} T cells, were all elevated by dual EP2 and EP4 inhibition (Figure S7D). In addition to the AT3 model, the effectiveness of dual EP2/EP4 inhibition in mitigating lung metastasis was further validated in 4T1 and E0771 transplantation models, representative of triple negative and luminal B breast cancer subtypes, respectively (Le Naour et al., 2020; Pulaski and Ostrand-Rosenberg, 2001) (Figures S7E and S7F), as well as in the MMTV-PyMT model (Figures 7B and 7C). Therefore, targeting both EP2 and EP4 was effective to control lung metastasis of breast cancer.

Next, we tested whether blockade of COX-2-PGE2-EP receptor signaling could reverse exogenous DC suppression and thereby improve the therapeutic efficacy of DC vaccines. After validating the effectiveness of the IV injection route to deliver ovalbumin (OVA)-pre-loaded BM-DCs (DC vaccine) (Figures S7G and S7H), we compared the efficacy of IV administered DC vaccine in treating lung metastasis in WT versus *Ptgs2*$^{\Delta Fb}$ mice using an experimental metastasis model induced by AT3-OVA-Luc cells, which expressed the OVA antigen (Figure 7D, left). Accompanied by higher numbers of circulating OVA-specific CD8^{+} T cells in *Ptgs2*$^{\Delta Fb}$ mice than in WT mice, DC vaccine was shown to be therapeutically effective in reducing lung metastases in *Ptgs2*$^{\Delta Fb}$ mice, but not in WT

mice (Figure 7D). However, the elevation of activated T cells by *Ptgs2* cKO was not detected in tumor- or lung-draining lymph nodes (Figure S7I), suggesting that lymph node stromal COX-2 signaling is likely not involved in modulation of exogenous DC functions. Recapitulating the result from genetic deletion of COX-2, dual inhibition of EP2 and EP4 similarly improved the therapeutic efficacy of DC vaccine as reflected by increased circulating OVA-specific $CD8^+$ T cells and mitigated lung metastasis (Figure 7E). Thus, blockade of the COX-2-PGE2-EP2/EP4 signaling pathway improved the therapeutic potential of DC vaccine in treating lung metastasis.

Furthermore, we speculated that eradication of the immunosuppressive lung microenvironment through targeting of lung stromal signaling would enhance efficacy of immune checkpoint blockade, which is known to be undermined when tumors have robust immunosuppressive microenvironments (Saleh and Elkord, 2020). Indeed, administration of anti-PD-1 did not have a significant effect in alleviating established lung metastases in the AT3 model in WT mice, whereas it was effective in $Ptgs2^{\Delta Fb}$ mice (Figure 7F). Furthermore, the combination of anti-PD-1 with dual inhibition of EP2 and EP4 was more effective than anti-PD-1 alone, reducing the metastatic burden by approximately 20 times compared to untreated controls (Figure 7G). Taken together, targeting lung fibroblast-associated COX-2-PGE2-EP2/4 signaling represents an effective means to treat breast cancer lung metastasis, as well as a promising combination therapy in synergy with immunotherapies for lung metastasis management.

Discussion

Despite numerous reports describing metastasis-promoting roles of BM-derived myeloid cells, little is known about whether these cells are intrinsically tumor-regulatory or acquire such capacities when they infiltrate organs. From the perspective of clinical translation, understanding tissue-specific immunity is critical for designing precise and effective therapeutics to treat organotropic metastases. In the present study, we found that exogenously implanted myeloid cells became dysfunctional or immunosuppressive only in the lung and not in any of several other tissues examined, indicating that immune cells can be reprogrammed in a distinct manner that depends on the tissue environment into which they are transmitted. Thus, our results will stimulate further studies on organ-specific immune responses in controlling organotropic metastases.

Stromal-immune cell interactions have drawn increasing attention in immunological research (Davidson et al., 2021; Koliaraki et al., 2020). During tissue homeostasis and tissue damage repair in various types of immunological diseases, structural stromal cells such as fibroblasts and endothelial cells are known to play fundamental roles in instructing immune cell development, survival, trafficking and function. With high-throughput sequencing technologies, stromal-immune cell interactions have started to be investigated at the single cell and tissue-specific levels (Buechler et al., 2021; Krausgruber et al., 2020). A growing number of such studies have focused on tissue homeostasis and immune diseases, whereas stromal-immune cell interactions remain less well characterized in cancer. Our results, by revealing $COX\text{-}2^+$ fibroblast-mediated reprogramming of diverse myeloid cells in the lung pre-metastatic niche, suggest that targeting organ stromal cells could be a more efficient

strategy to reshape an immune microenvironment than targeting a single population of myeloid cells in metastasis treatment.

COX-2 inhibitors have been proposed as promising therapeutics in breast cancer management (Mazhar et al., 2006; Regulski et al., 2016). However, some clinical trials using COX-2 inhibitors, such as the European Celecoxib Trial in Primary Breast Cancer (REACT), have not shown significant benefit for breast cancer patients (Coombes et al., 2021; Hamy et al., 2019; Hawk et al., 2018; Strasser-Weippl et al., 2018). This is also reflected in our mouse finding that celecoxib was ineffective in controlling lung metastasis of breast cancer. It is plausible that pharmacological inhibition of COX-2 may not be sufficient to reduce tissue-resident PGE2 levels due to compensatory effects by the COX-1 isoform. In our study, *Ptgs2* cKO significantly reduced lung tissue PGE2 levels at both naïve and tumor-bearing states. We posit that this might be due to the *de novo* nature of the fibroblast *Ptgs2* deletion, which further disrupts the fibroblast COX-2-PGE2-dependent induction of *Ptgs2* expression in myeloid cells. Based on our results from mouse breast cancer models, blockade of PGE2 receptors, which remains less explored in clinical settings than inhibition of COX enzymes (Pannunzio and Coluccia, 2018; Reader et al., 2011), could be an effective approach in prevention and treatment of lung metastasis. Emerging data from multiple mouse models of solid cancers have shown promising effects from the combination of EP4 antagonists and PD1/PD-L1 blockade in inhibiting primary tumor growth (Lu et al., 2021; Peng et al., 2022; Sajiki et al., 2020; Tokumasu et al., 2022; Wang et al., 2021). In our work, dual inhibition of EP2 and EP4 was required to suppress lung metastasis, possibly owing to the potent immunosuppressive lung microenvironment. The preclinical efficacy of the combination of EP2 and EP4 inhibition with either DC vaccine or immune checkpoint inhibitor in our work is expected to stimulate translational studies of their application with immunotherapies to treat metastatic disease.

Given that the COX-2^+ lung fibroblast program acts to remodel the lung microenvironment even in the absence of distal primary tumors, we expect that our results will also have relevance to a broad range of immune-associated pathologies other than metastasis, such as primary lung tumors, interstitial lung disease, and pulmonary infections. In these pathological conditions, abnormalities of the innate and adaptive immune responses, excessive inflammation, and immunosuppression are major challenges from the standpoint of both mechanistic understanding and clinical treatment (Desai et al., 2018; Iams et al., 2020; Mizgerd, 2012). However, the underlying mechanisms driving these challenges remain poorly characterized, and current immune-based therapies are largely limited to targeting a single or a few types of immune cells (Goswami et al., 2022; Kolahian et al., 2016). Based on our findings, resident stromal cells, and in particular fibroblasts, represent a master switch in the lung immune microenvironment which broadly reshapes the lung immune landscape. Pharmacological targeting of lung stromal factors, such as COX-2-PGE2, is a promising avenue in the treatment of the immune-associated lung diseases.

Limitations of the study

In this work, we mainly relied on immunofluorescence, single cell and bulk RNA-seq, exogenous myeloid cell transplantation, and *ex vivo* co-cultures. The *in situ* molecular

mechanisms and cell-cell interaction dynamics of COX-2$^+$ AdvF-elicited reprograming of different lung-resident myeloid cells at spatial-temporal levels should be further investigated by leveraging currently advancing spatial transcriptomics and metabolomics approaches, as well as intravital imaging techniques. In addition, we characterized the role of COX-2$^+$ AdvFs only in the context of lung metastasis models; future efforts will be required to more fully understand this lung fibroblast subset in maintaining lung-resident immunity in homeostasis, inflammation, lung cancer and other lung diseases.

STAR★METHODS

RESOURCE AVAILABILITY

Lead Contact—Information and requests for resources and reagents should be directed to and will be fulfilled by the Lead Contact, Guangwen Ren (Gary.Ren@jax.org).

Materials Availability—All unique and stable materials generated in this study are available from the Lead Contact under a Materials Transfer Agreement.

Data and Code Availability

- Bulk RNA-seq and scRNA-seq data generated from this study were deposited in public data repositories and the accession numbers are listed in the KEY RESOURCES TABLE. All these data are publicly available as of the date of publication.
- This paper does not report original code.
- Any additional information required to reanalyze the data reported in this paper is available from the lead contact upon reasonable request.
- The following datasets were downloaded and reanalyzed: microarray datasets for human normal tissues: GSE7307 and GSE3526 (Roth et al., 2006); scRNA-seq datasets for human idiopathic pulmonary fibrosis samples: GSE135893 (Habermann et al., 2020); scRNA-seq datasets for human lung tissues: EGAS00001004344 (Travaglini et al., 2020).

EXPERIMENTAL MODEL AND SUBJECT DETAILS

Animals—BALB/cJ (JAX #000651), C57BL/6J (JAX #000664), B6.SJL-*Ptprc*^{a} *Pepc*^{b}/BoyJ (B6 Cd45.1, JAX #002014), C57BL/6-Tg (TcraTcrb)1100Mjb/J (OT-I, JAX #003831), B6.Cg-Tg(TcraTcrb)425Cbn/J (OT-II, JAX #004194), B6;129S-*Ptgs2*^{tm1Jed}/J (*Ptgs2*$^{-/-}$, JAX #002476), B6;129S4-*Ptgs2*$^{tm2.1Hahe}$/J (*Ptgs2*^{Luc}, JAX #030853), B6;129S4-*Ptgs2*^{tm1Hahe}/J (*Ptgs2* $^{flox/flox}$, JAX #030785), C57BL/6-Tg(*Pdgfra*-cre)1Clc/J (*Pdgfra*^{Cre}, JAX #013148), B6.129S4-*Pdgfra*$^{tm11(EGFP)Sor}$/J (*CD140a*^{EGFP}, JAX #007669), B6.129S7-*Il1r1*^{tm1Imx}/J (*Il1r1*$^{-/-}$, JAX #003245), FVB/N-Tg(MMTV-PyVT)634Mul/J (JAX #002374) and MMTV-PyMT (B6.FVB-Tg(MMTV-PyVT)634Mul/LellJ (JAX #022974) mice were all obtained from The Jackson Laboratory. B6;129S4-*Ptgs2*^{tm1Hahe}/J (*Ptgs2* $^{flox/flox}$) and C57BL/6-Tg(*Pdgfra-cre*)1Clc/J (*Pdgfra*^{Cre}) mice were crossed to generate *Ptgs2* conditional knockout (*Ptgs2*$^{\Delta Fb}$) mice. The *Ptgs2*$^{\Delta Fb}$ mice were further crossed with MMTV-PyMT (B6.FVB-Tg(MMTV-PyVT)634Mul/LellJ) mice to generate *Pdgfra*^{Cre}; *Ptgs2*$^{flox/flox}$; MMTV-PyMT

(MMTV-PyMT *Ptgs2*$^{\Delta Fb}$) mice. Animal handling and experimental protocols were reviewed and approved by the Institutional Animal Care and Use Committee of The Jackson Laboratory.

Female mice aged 8–10 weeks were used unless indicated otherwise. For all animal work, mice with similar age and weight were randomized before tumor inoculation. Prior to further treatment, the tumor-bearing mice were randomized with respect to their tumor sizes to ensure all treatment groups had equivalent tumor burden before treatment. All animal experiments were performed in the same well-controlled pathogen-free facility with the same mouse diets.

Cell lines—4T1 and YAC-1 cells were purchased from the ATCC. E0771 cells were purchased from CH3 Biosystems. AT3 cell line was a generous gift from S.I. Abrams at Roswell Park Comprehensive Cancer Center. To generate AT3-Luc, E0771-Luc or 4T1-Luc cells, the tumor cells were infected with luciferase-expressing lentivirus (Addgene) (Campeau et al., 2009). For OVA labeling, the AT3-Luc cells were transfected with pcDNA3-OVA (Addgene) (Diebold et al., 2001) to generate AT3-OVA-Luc tumor cells. For mCherry labeling, AT3 cells were infected with mCherry-expressing lentivirus (Addgene) to generate AT3-mCherry cells. To overexpress G-CSF, AT3 cells were infected with *g-csf* (*Csf3*)-expressing lentivirus (the vector was a gift from R.A. Weinberg, Massachusetts Institute of Technology) to generate AT3-*gcsf* cells. To generate 4T1-GFP, AT3-GFP, AT3-*gcsf*-GFP and E0771-GFP cells, the tumor cells were infected with green fluorescent protein (GFP)-expressing lentivirus (Addgene). Human lung fibroblast-like cells (mesenchymal stem cells) were purchased from ScienCell Research Laboratories. All cell lines were maintained in a humidified 5% CO_2 incubator at 37 °C and confirmed to be mycoplasma free.

Generation of BM-DCs—Bone marrow cells from naïve mice were isolated by flushing femurs, tibias and humeri with RPMI-1640 supplemented with 10% fetal bovine serum (FBS) and 1% penicillin-streptomycin. Following suspension in ammonium-chloride-potassium (ACK) lysis buffer to lyse red blood cells, bone marrow cells were passed through a 40 μm filter. Then cells were resuspended at a density of 1×10^6 cells per ml, cultured in complete RPMI-1640 medium containing GM-CSF (20 ng/ml) and IL-4 (10 ng/ml). The cultured medium was entirely discarded on day 4 and new warmed medium supplemented with GM-CSF and IL-4 was added. On day 7, the loosely-adherent cells were collected for further experiments.

To screen the lung fibroblast-derived candidate soluble factors to modulate BM-DCs, BM-DCs were treated with the candidate regulators for 16 hours and then MHC-II expression levels in BM-DCs were measured by flow cytometry. The final concentration of each following reagent was used at 10 ng/ml unless indicated otherwise: β-estradiol, interleukin 6 (IL-6), interleukin 2 (IL-2), hepatocyte growth factor (HGF), interleukin 33 (IL-33), interleukin 13 (IL-13), PGE2, interleukin 4 (IL-4), tretinoin, platelet-derived growth factor BB (PDGF-BB), progesterone, and interleukin 10 (IL-10).

To determine the impact of tissue environments on BM-DCs *in vivo*, naïve mice or orthotopic tumor-bearing mice (pre-metastatic stage) were IV injected with CellTracker™ orange dye (Thermo Fisher Scientific) labeled BM-DCs (5×10^6 cells for each mouse). 16 hours later, mice were euthanized, and different tissues and organs were harvested for detection of the labeled BM-DCs and their expression of MHC molecules by flow cytometry.

Primary cell isolation and culture—Splenic $CD3^+$ T cells or NK cells were isolated from naïve mice using anti-CD90.2 magnetic beads (Miltenyi Biotec) or NK cell isolation kit (Miltenyi Biotec) according to the manufacturer's instructions. Splenic $CD4^+$ or $CD8^+$ T cells were isolated from naïve OT-II or OT-I mice by using CD4 (L3T4) or CD8a (Ly-2) microbeads (Miltenyi Biotec), respectively. BM-derived monocytes were isolated from naïve mice using the Monocyte Isolation Kit (Miltenyi Biotec) following the manufacturer's protocol. Neutrophils were isolated from lung tissues of naïve or tumor-bearing mice using anti-Ly6G microbeads (Miltenyi Biotech). Viability and purity of isolated cells were assessed with flow cytometry to be above 90%.

For the primary culture of lung fibroblasts, sorted $CD45^-CD31^-CD326^-CD140a^+$ fibroblasts were cultured in the MesenCult™ Basal Medium (STEMCELL Technologies). The first to third passages of the primary fibroblasts were used for the *ex vivo* experiments.

To prepare fibroblast-derived conditioned medium (CM), *ex vivo* cultured lung fibroblasts or freshly sorted lung $CD140a^+$ fibroblasts were cultured in RPMI-1640 medium at a density of 5×10^5 cells/ml for 16 hours. Then the supernatant was collected after centrifuging at 1, 000*g* for 20 min to remove cells and debris. The freshly collected supernatant was used as CM for further experiments.

Tissue dissociation—Peripheral blood (PB) was collected through cardiac puncture in 5 mM EDTA in PBS with 1 ml syringe. Then PB samples were lysed with ACK lysis buffer for 5 min and centrifuged. Cells were filtered through a 40-μm strainer and resuspended in RPMI-1640 supplemented with 5% FBS. For BM cells, the tibias and femurs of both hind legs of the mice were flushed with RPMI-1640 medium. Then cells were lysed with ACK lysis buffer and passed through a 40-μm strainer. Lungs and livers were extracted and minced, and then digested with 2 mg/ml collagenase IV (Thermo Fisher Scientific) and 0.1 mg/ml DNase I (Sigma) in RPMI-1640 medium for 1 hour at 37 °C. The cells were then filtered through 70-μm strainers to remove small fragments of undigested tissue. Spleens were harvested and ground with syringe plungers and the cell suspensions were filtered through 70-μm strainers. For lung, liver and spleen, the red blood cells were lysed using ACK lysis buffer and then homogenized into single cell suspensions with 40-μm strainers.

Flow cytometry and sorting—Prepared single cell suspensions from mouse tissues or *ex vivo* cultured cells were stained on ice with primary fluorophore conjugated antibodies (1:200 diluted) and then washed with FACS buffer (PBS supplemented with 2% FBS) for identification of cell populations by flow cytometry. 4,6-diamidino-2-phenylindole (DAPI) was used for dead cell discrimination. For the intracellular staining of COX-2, single-cell suspensions were first stained with Live/Dead Fixable stain BV510 (Thermo Fisher

Scientific) and surface primary antibodies, then fixed and permeabilized using Cytofix/Cytoperm kit (BD Biosciences) according to the manufacturer's instructions. Cells were then stained with primary antibody against COX-2 (1:500 diluted) for 2h on ice followed with secondary antibody (1:1000 diluted) staining for 1 hour at 4°C. IgG was stained as negative control for flow cytometry gating. Then the samples were washed and analyzed by flow cytometry. For cell counting on the flow cytometer, Precision Count Beads™ (Biolegend) were utilized to obtain the absolute counts of cells of interest in each lung tissue according to the manufacturer's instructions.

Flow cytometry was performed on a FACSymphony A5 cytometer (BD Biosciences) and the data were analyzed using FACSDiva software (BD Biosciences) and FlowJo software (BD Biosciences). Cell sorting was performed on the BD FACSAria II cell sorter with a 100 μm nozzle. All antibodies were purchased from either Biolegend or BD Biosciences. Detailed information regarding antibodies is listed in the KEY RESOURCES TABLE.

Determination of the pre-metastatic stages of breast tumor models—Flow cytometry was used to determine the pre-metastatic versus metastatic stages for the breast cancer models (4T1, AT3, AT3-*gcsf* and E0771). Using 4T1 model as an example, the mice were orthotopically implanted with 4T1-GFP tumor cells (5×10^5 cells for each mouse), and on days 10, 15, 20 and 25, the percentages of tumor cells in the mouse lungs were quantified by flow cytometry. Primary tumor tissues and naïve mice-derived lung samples (day 0) were set as positive or negative controls, respectively. The pre-metastatic stage was designated as a period before overt metastasis occurs in distant lung tissues, when either no or very few tumor cells were detected. In addition to the flow cytometry method, the evidence of metastasis in the lung was also validated by histological examination. Accordingly, we identified day 15 or earlier as the pre-metastatic stage for the 4T1 model. Similarly, the pre-metastatic stages for AT3, AT3-*gcsf* and E0771 models are day 15 or earlier, day 15 or earlier, and day 20 or earlier, respectively.

DC functional assays—To measure the antigen-specific T cell priming ability, BM-DCs were pre-incubated with $OVA_{257\text{-}264}$ or $OVA_{323\text{-}339}$ peptide (1 μg/ml) at 37°C for 2 hours before washing. Then the BM-DCs were co-cultured with carboxyfluorescein succinimidyl ester (CFSE)-labelled OT-I $CD8^+$ T cells or OT-II $CD4^+$ T cells at a ratio of 1:3 for 3 days. T cell proliferation was assessed by flow cytometry.

To assess the antigen uptake ability, BM-DCs were incubated with OVA-Alexa Fluor 647 (0.1 μg/ml) at 37°C for 1 hour. Cells were then washed and stained with antibodies and presence of Alexa Fluor 647 signal was analyzed by flow cytometry in BM-DCs.

To measure the immunosuppressive ability, BM-DCs were pre-incubated with WT or *Ptgs2*$^{-/-}$ lung fibroblast CM for 16 hours, and mixed with untreated BM-DCs (pre-loaded with $OVA_{257\text{-}264}$ or $OVA_{323\text{-}339}$ peptide) at a ratio of 1:1. Then the CFSE-labelled naïve splenic T cells (from OT-1 or OT-II mice) were added (CM-treated BM-DCs : antigen-loaded BM-DCs : T cells=1:1:3) and co-cultured for 3 days. T cell proliferation was assessed by flow cytometry.

Monocyte-mediated T cell suppression assay—To measure the T cell suppression by monocytes, BM-derived monocytes were pre-incubated with WT or *Ptgs2*$^{-/-}$ lung fibroblast CM for 24 hours before washing. Splenic CD3^{+} T cells were isolated from naive mice and labeled with CFSE. Then monocytes (2×10^5 cells) were co-cultured with T cells (5×10^5 cells) in the presence of anti-CD3/CD28 beads (Dynabeads Mouse T-Activator CD3/28, Thermo Fisher Scientific) for 3 days at 37°C. T cell proliferation was assessed by flow cytometry.

***In vitro* NK cell cytotoxicity assay—**BM-DCs or BM-derived monocytes were pre-treated with lung fibroblast CM for 24 hours, and co-cultured with 2×10^5 purified splenic NK cells at a ratio of 1:1 for 2 hours in a 96-well round bottom plate. CellTracker™ deep red dye (Thermo Fisher Scientific) labeled YAC-1 target cells were then added at the NK cell: target cell ratio of 5:1 and co-cultured for an additional 4 hours. The cells were stained with propidium iodide (PI) and the percentage of dead target cells was measured with flow cytometry.

Immunofluorescence—To determine the localization of implanted BM-DCs and lung-resident fibroblasts in the lung, *CD140a*^{EGFP} mice were IV injected with CellTracker™ orange dye (Thermo Fisher Scientific) labeled BM-DCs (5×10^6 cells for each mouse). 16 hours later, the lungs were dissected and fixed with 4% paraformaldehyde (PFA). Then the tissues were embedded in OCT compound (Tissue-Tek) and tissue sections (10 μm) were prepared with the CryoStar NX70 (Thermo Fisher Scientific). The cell nucleus was stained with DAPI.

To detect COX-2 protein level, the lung CD140a^{+} fibroblasts from WT or *Ptgs2*$^{\Delta Fb}$ mice, or vehicle or IL-1β treated lung fibroblasts were first fixed with 4% PFA at room temperature for 30 min. Then the cells were washed with PBS three times, and incubated with COX-2 primary antibody (1:1000 diluted) overnight at 4°C. The next day, the cells were washed with PBS and then incubated with conjugated secondary antibody (1:1000 diluted) for 1 hour at room temperature. Finally, the cells were stained with DAPI (1 μg/ml) to label the cell nucleus.

To determine the localization of COX-2^{+} fibroblasts and their *in situ* interactions with different types of myeloid cells, the lungs of *CD140a*^{EGFP} mice were harvested and fixed with 4% PFA. Then the tissues were embedded in OCT compound and sectioned at 10 μm. Cryosections were permeabilized with 0.1% Triton, blocked with 5% BSA, and stained with primary antibodies overnight at 4°C. The following antibodies were used to indicate different types of myeloid cells: myeloid cells (CD45 and CD11b), CD11b^{+} DCs (CD11b and CD172a), CD103^{+} DCs (CD11c and XCR1), monocytes (Ly6C), and neutrophils (Ly6G). The next day, the lung sections were stained with secondary antibodies (diluted 1:500) for 1 hour at room temperature. All the antibody information is listed in the KEY RESOURCES TABLE. The fluorescent images were captured on a Leica SP8 confocal microscope (Leica).

Quantification of PGE2 and IL-1β—To measure the soluble PGE2 levels in different lung stromal cells, 5×10^4 sorted cells were seeded in a well of a 96-well plate and

cultured overnight. To measure the lung-resident PGE2 level, fresh bronchoalveolar lavage fluid (BALF) was rapidly harvested by using HBSS solution gently instilled into the lung through the trachea and then carefully retracted to maximize BALF retrieval. The BALF was then centrifuged at 300g to remove cell pellets, and the supernatant was collected for PGE2 measurement. To measure the IL-1β production in lung neutrophils, isolated neutrophils from naïve mice or tumor-bearing mice were seeded in a 96-well plate at the density of 5×10^4 cells per well and cultured overnight. On the next day, the conditioned medium was collected and centrifuged to remove any cells and debris. The concentration of PGE2 or IL-1β in supernatants was measured by using the Prostaglandin E2 Parameter Assay Kit (R&D Systems) or Mouse IL-1 beta/IL-1F2 Quantikine ELISA Kit (R&D Systems), respectively, following the manufacturer's instructions.

Western blot—Fibroblasts were harvested at 4° C in RIPA lysis buffer (Sigma) in the presence of protease inhibitor cocktail (Sigma). The protein samples were subjected to 4-20% Tris-Glycine gels (Thermo Fisher Scientific), and after electrophoresis for 1 hour, they were transferred to nitrocellulose membranes (Bio-Rad). The membranes were probed overnight at 4° C with antibodies specific for COX-2 and GAPDH after blocking with 5% blotting-grade blocker (Bio-Rad). Then HRP-conjugated secondary antibodies were added and incubated for 1 hour at room temperature and finally the membrane-bound immune complexes were detected with Pierce ECL Plus Substrate (Thermo Fisher Scientific).

RNA extraction and RT-qPCR—Total RNA was extracted from cells using the Direct-zol RNA Miniprep Plus Kits (Zymo Research) according to the manufacturer's instructions. Reverse transcription was conducted with High-Capacity cDNA Reverse Transcription Kit (Thermo Fisher Scientific). Real-time quantitative PCR (RT-qPCR) was carried out with the ViiA 7 Real-Time PCR system (Thermo Fisher Scientific) using the PowerUp SYBR™ Green PCR Master Mix (Thermo Fisher Scientific). Relative gene expression was calculated using the comparative cycle method ($2^{-\Delta\Delta Ct}$) normalized to the housekeeping gene *Rps18*. Primer sequences are listed in Table S1.

RNA sequencing—For the RNA-seq of BM-DCs, total RNA was extracted from BM-DCs after treatment with WT or *Ptgs2*$^{-/-}$ lung fibroblast CM, or PGE2 (10 ng/ml) for 16 hours. For the RNA-seq of lung fibroblasts, total RNA was extracted from fibroblasts after treatment with IL-1β (10 ng/ml) for 24 hours. For the RNA-seq of lung myeloid cells, CD11b$^+$ DCs, CD103$^+$ DCs and conventional monocytes were sorted from WT or *Ptgs2*$^{\Delta Fb}$ naïve mice. Total RNA isolation, sample quality check and library preparation were performed by the Genome Technologies core facility at The Jackson Laboratory. After the quality check, libraries were pooled and sequenced, 100-bp paired-end on the HiSeq 4000 (Illumina) by using HiSeq 3000/4000 SBS kit reagents (Illumina). Paired-end reads were aligned to Mus musculus reference GRCm38. The transcripts per million (TPM) results of RNA-seq data were used in the limma package (version 3.46.0) (Ritchie et al., 2015) to determine differentially expressed genes. Ingenuity Pathway Analysis (QIAGEN) was used to predict candidate upstream regulators.

Single cell sequencing preparation—Lung stromal cells ($CD45^-CD31^-CD326^-$) were sorted from naïve C57BL/6J mice, and $CD140a^+$ fibroblasts ($CD45^-CD31^-CD326^-$ GFP^+) were sorted from naïve *CD140a*^{EGFP} mice. Lung $CD45^+$ immune cells were sorted from WT or *Ptgs2*$^{\Delta Fb}$ naïve mice. Single cell capture, barcoding and library preparation were performed by the Single Cell Biology core facility at The Jackson Laboratory with the 10x Chromium system using version 2 chemistry, following the manufacturer's instructions (10x Genomics). Approximately 12,000 cells were loaded into one lane of a 10x Chromium microfluidic chip. Following capture and lysis, cDNA was synthesized and amplified, and the amplified cDNA was used to construct an Illumina sequencing library. The generated libraries were checked for quality, and then sequenced by using the Illumina HiSeq 4000. A median sequencing depth of 50,000 reads per cell was targeted for each sample.

Single cell RNA sequencing analysis—Downstream analysis of the scRNA-Seq data was performed by using Seurat (Stuart et al., 2019). For lung stromal cells ($CD45^-CD31^-CD326^-$) from naïve C57BL/6J mice, data from 6,776 cells with 32,285 genes were obtained after passing the CellRanger's quality control steps. 21,584 genes were retained after removal of the genes expressed in less than one cell. 6,237 cells were retained after removing low quality cells. For $CD140a^+$ fibroblasts from the naïve *CD140a*^{EGFP} mice, data from 4,796 cells with 31,053 genes were obtained after passing the CellRanger's quality control steps. 19,363 genes were retained after removal of the genes expressed in less than one cell. 4,640 cells were retained after removing low quality cells.

Read counts were normalized using 'LogNormalize' method. Variable genes were detected using the Seurat function FindVariableFeatures with default parameters. The data were then scaled, and principal component analysis (PCA) was performed for dimensionality reduction. The first 20 principal components (PCs) were used as input for a graph-based approach to cluster cells by cell type and as input to t-SNE for reduction to two dimensions to facilitate visualization. The Seurat function FindAllMarkers with default parameters was used to identify marker genes when comparing every cluster to all remaining cells. Avg-logFC was chosen to represent the cluster-specific markers and top 10 markers of each cluster were calculated with default parameters. The Seurat function DoHeatmap was used for plotting the top 10 markers for each cluster in $CD140a^+$ fibroblasts, and the output figure (Figure 3D) lacked some genes (*Tagln* in cluster 4; *Rgs2*, *Npnt* and *Limch1* in cluster 5) as this function currently did not support plotting the same gene multiple times in the heatmap. The full top 10 marker genes were shown on the right side of heatmap in Figure 3D. The enrichment analysis for Gene Ontology terms in *Ptgs2*^{hi} fibroblasts was performed using Metascape (Zhou et al., 2019), and the transcription factor (TF) activities were analyzed with DoRothEA (version 1.1.2) (Holland et al., 2020).

***Ex vivo* bioluminescence imaging (BLI)—**For *Ptgs2*^{Luc} reporter mice, the luciferase signals in different tissues and organs were measured by BLI to determine the constitutive expression of *Ptgs2*. For metastasis models used in the present study, the luciferase activities in lungs were used to monitor lung metastasis progression. The mice were euthanized, and tissues and organs were rapidly dissected and placed in a 24-well plate filled with 2 ml D-luciferin (150 μg/ml; diluted in PBS) for *ex vivo* BLI.

BLI results were obtained using the Xenogen IVIS system. Light emission from the region of interest was quantified as photons/second/cm^2/steradian (p/sec/cm^2/sr) through Living Images software.

Experimental lung metastasis models—To detect lung metastasis progression in WT or *Ptgs2*$^{\Delta Fb}$ mice, mice were first orthotopically implanted with 5 × 10^5 AT3 (or E0771) tumor cells. On day 12, the luciferase-labeled AT3-Luc (or E0771-Luc) cells were IV injected (5 × 10^5 cells for each mouse). On day 26, mice were euthanized, and the lungs were rapidly harvest for *ex vivo* BLI.

To detect the effect of DC depletion on metastasis in *Ptgs2*$^{\Delta Fb}$ mice, the mice were first orthotopically implanted with 5 × 10^5 AT3 tumor cells. From day 5 to day 25, the mice were IV injected with control liposomes or clodronate-loaded liposomes every four days (150 μl for each mouse). On day 11, the luciferase-labeled AT3-Luc cells were IV injected (5 × 10^5 cells for each mouse). On day 28, mice were euthanized, and the lungs were rapidly harvested for *ex vivo* BLI.

To detect the therapeutic efficacy of DC vaccines in WT or *Ptgs2*$^{\Delta Fb}$ mice, the mice were orthotopically implanted with 5 × 10^5 AT3 tumor cells. 7 days later, mice were IV injected with OVA-expressing AT3-Luc tumor cells (AT3-OVA-Luc, 5 × 10^5 cells for each mouse). On day 16, DC vaccines were prepared: BM-DCs were incubated with 100 ng/ml $OVA_{257\text{-}264}$ peptide at 37° C for 1 hour. BM-DCs without OVA loading were used as a control. Cells (5 × 10^5 cells for each mouse) were then washed extensively in PBS and IV injected into tumor-bearing WT or *Ptgs2*$^{\Delta Fb}$ mice. On day 23, H-2K^b/SIINFEKL MHC pentamers (ProImmune) were used for the detection of OVA-specific CD8$^+$ T cells in the blood. On day 28, mice were euthanized, and the lungs were rapidly harvested for *ex vivo* BLI.

To detect the therapeutic efficacy of anti-PD-1 immunotherapy in WT or *Ptgs2*$^{\Delta Fb}$ mice, mice were first orthotopically implanted with 5 × 10^5 AT3 tumor cells. On day 7, the luciferase-labeled AT3-Luc cells were IV injected (5 × 10^5 cells for each mouse). From day 15 to day 24, the mice were intraperitoneally (IP) injected with isotype or anti-PD-1 (10 mg/kg) every 3 days (total 4 times). On day 26, mice were euthanized, and the lungs were rapidly harvested for *ex vivo* BLI.

To detect the therapeutic potency of the COX-2 inhibitor (Celecoxib), EP2 antagonist (PF-04418948) or/and EP4 antagonist (MF498) in treating lung metastasis, mice were first orthotopically implanted with 5 × 10^5 tumor cells (AT3, 4T1 or E0771). From day 5 to day 13, the mice were IP injected with vehicle or inhibitor or antagonists (10 mg/kg) daily. On day 9, the luciferase-labeled tumor cells were IV injected (5 × 10^5 cells for each mouse). On day 26, mice were euthanized, and the lungs were rapidly harvested for *ex vivo* BLI.

To detect the combined effect of the dual inhibition of EP2 and EP4 and DC vaccine, mice were first orthotopically implanted with 5 × 10^5 AT3 tumor cells. On day 7, mice were IV injected with AT3-OVA-Luc cells (5 × 10^5 cells for each mouse). From day 12 to day 20, the mice were IP injected with vehicle or antagonists (10 mg/kg) daily. On day 16, the

DC vaccine (BM-DCs loaded with OVA antigen) or control DCs (BM-DCs without OVA loading) were IV injected (5×10^5 cells for each mouse). On day 23, H-2K^b/SIINFEKL MHC pentamers (ProImmune) were used for the detection of OVA-specific CD8$^+$ T cells in the blood. On day 28, mice were euthanized, and the lungs were rapidly harvested for *ex vivo* BLI.

To detect the combined effect of the dual inhibition of EP2 and EP4 and anti-PD-1 immunotherapy, mice were first orthotopically implanted with 5×10^5 AT3 tumor cells. On day 7, the luciferase-labeled AT3-Luc cells were IV injected (5×10^5 cells for each mouse). From day 15 to day 24, the mice were IP injected with anti-PD-1 (10 mg/kg) every 3 days, or EP2 and EP4 antagonists (10 mg/kg) daily, or the combination of both. On day 26, mice were euthanized, and the lungs were rapidly harvested for *ex vivo* BLI.

Spontaneous lung metastasis models—For spontaneous metastasis model in WT or *Ptgs2*$^{\Delta Fb}$ mice, mCherry labelled AT3 (AT3-mCherry) tumor cells were injected into the fourth mammary fat pads of female WT or *Ptgs2*$^{\Delta Fb}$ mice. On day 16, primary tumors were surgically resected. On day 30, mice were euthanized, and the lungs were harvested for flow cytometry or immunofluorescence analysis to determine the percentage of mCherry$^+$ tumor cells.

For spontaneous metastasis model in WT MMTV-PyMT or MMTV-PyMT *Ptgs2*$^{\Delta Fb}$ mice, 6-month-old female mice with spontaneous mammary tumors were euthanized, and spontaneous lung metastases were detected by histological analysis and macroscopic examination.

To detect the combined effect of the dual inhibition of EP2 and EP4 in the genetically engineered MMTV-PyMT model, 10-week-old female MMTV-PyMT mice (FVB background; JAX #002374) were randomized to two groups when palpable mammary tumors were first detected. The mice received IP injection of both EP2 and EP4 antagonists (10 mg/kg) or vehicle every 3 days. A month after the first treatment, the mice were euthanized, and spontaneous lung metastases were detected by histological analysis, macroscopic examination or qPCR analysis.

BM chimera assay—BM-derived cells from sex- and aged-matched donor mice (B6 CD45.1 mice) were obtained by flushing femurs and tibias. Within 24 hours after irradiation with 900 cGy, CD45.2 recipient mice (WT or *Ptgs2*$^{\Delta Fb}$ mice) were IV injected with 1×10^7 BM cells from CD45.1 donor mice. Three months later, the chimeric mice were validated for successful BM transplantation.

Illustration Tool—The schematic images are created with BioRender.com.

QUANTIFICATION AND STATISTICAL ANALYSIS

The details of the replicates for each experiment are listed in the respective figure legends. In brief, unless otherwise indicated, for most *in vitro* or *ex vivo* studies, the data shown are representative of at least five independent experiments, and for most *in vivo* studies, the data shown are representative of at least three independent experiments. Conclusions from

the repeated experiments that are not shown in the manuscript are the same as those from the shown experiments. The sample size in each experiment was determined based on the level of expected heterogeneity of the samples, the significance threshold (chosen at 0.05), the expected or observed difference, as well as previous publications and our pilot studies. The chosen sample size in each experiment is sufficient to generate statistically significant results. In all experiments, data are shown as mean ± SEM, and statistical analyses were performed using GraphPad Prism software (version 8.2.1). Statistical significance between two groups was calculated using an unpaired two-tailed Student's t-test, Mann–Whitney test or Wilcoxon test, as indicated in figure legends. One-way ANOVA with multiple comparisons test was used to compare the variance in more than two groups with one independent factor. When there were effects of two factors on a dependent variable, two-way ANOVA was performed. Statistical significance is defined as * $p < 0.05$, ** $p < 0.01$, *** $p < 0.001$, **** $p < 0.0001$, or NS (not significant).

Supplementary Material

Refer to Web version on PubMed Central for supplementary material.

Acknowledgments

We thank Dr. Scott I. Abrams (Roswell Park Comprehensive Cancer Center) for providing the AT3 cell line and thank Dr. Robert A. Weinberg (MIT) for providing the lentiviral vector expressing the mouse G-CSF. This work was supported by NIH grants (R00-CA188093, R37-CA237307, R01-CA251433, and P30-CA034196 to G.R., and R24-OD026440 to L.D.S.). Z.G. is supported by the Brooks Scholar Award Program at The Jackson Laboratory. We appreciate Dr. Iiro Taneli Helenius for his critical editing of the manuscript, Drs. Edison T. Liu, Karolina Palucka, Nadia A. Rosenthal, and David V. Serreze for their insightful advice during the project, and also thank the assistance from The Jackson Laboratory Scientific Service.

References

Altorki NK, Markowitz GJ, Gao D, Port JL, Saxena A, Stiles B, McGraw T, and Mittal V (2019). The lung microenvironment: an important regulator of tumour growth and metastasis. Nat Rev Cancer 19, 9–31. [PubMed: 30532012]

Baharom F, Rankin G, Blomberg A, and Smed-Sorensen A (2017). Human Lung Mononuclear Phagocytes in Health and Disease. Front Immunol 8, 499. [PubMed: 28507549]

Buechler MB, Pradhan RN, Krishnamurty AT, Cox C, Calviello AK, Wang AW, Yang YA, Tam L, Caothien R, Roose-Girma M, et al. (2021). Cross-tissue organization of the fibroblast lineage. Nature 593, 575–579. [PubMed: 33981032]

Campeau E, Ruhl VE, Rodier F, Smith CL, Rahmberg BL, Fuss JO, Campisi J, Yaswen P, Cooper PK, and Kaufman PD (2009). A versatile viral system for expression and depletion of proteins in mammalian cells. PLoS One 4, e6529. [PubMed: 19657394]

Coombes RC, Tovey H, Kilburn L, Mansi J, Palmieri C, Bartlett J, Hicks J, Makris A, Evans A, Loibl S, et al. (2021). Effect of Celecoxib vs Placebo as Adjuvant Therapy on Disease-Free Survival Among Patients With Breast Cancer: The REACT Randomized Clinical Trial. JAMA Oncol 7, 1291–1301. [PubMed: 34264305]

Dahlgren MW, and Molofsky AB (2019). Adventitial Cuffs: Regional Hubs for Tissue Immunity. Trends Immunol 40, 877–887. [PubMed: 31522963]

Davidson S, Coles M, Thomas T, Kollias G, Ludewig B, Turley S, Brenner M, and Buckley CD (2021). Fibroblasts as immune regulators in infection, inflammation and cancer. Nat Rev Immunol.

Desai O, Winkler J, Minasyan M, and Herzog EL (2018). The Role of Immune and Inflammatory Cells in Idiopathic Pulmonary Fibrosis. Front Med (Lausanne) 5, 43. [PubMed: 29616220]

Desch AN, Henson PM, and Jakubzick CV (2013). Pulmonary dendritic cell development and antigen acquisition. Immunol Res 55, 178–186. [PubMed: 22968708]

Diebold SS, Cotten M, Koch N, and Zenke M (2001). MHC class II presentation of endogenously expressed antigens by transfected dendritic cells. Gene Ther 8, 487–493. [PubMed: 11313828]

Doni A, Stravalaci M, Inforzato A, Magrini E, Mantovani A, Garlanda C, and Bottazzi B (2019). The Long Pentraxin PTX3 as a Link Between Innate Immunity, Tissue Remodeling, and Cancer. Front Immunol 10, 712. [PubMed: 31019517]

Funk CD (2001). Prostaglandins and leukotrienes: advances in eicosanoid biology. Science 294, 1871–1875. [PubMed: 11729303]

Gao Y, Bado I, Wang H, Zhang W, Rosen JM, and Zhang XH (2019). Metastasis Organotropism: Redefining the Congenial Soil. Dev Cell 49, 375–391. [PubMed: 31063756]

Gong Z, Li Q, Shi J, and Ren G (2022). An Artifact in Intracellular Cytokine Staining for Studying T Cell Responses and Its Alleviation. Front Immunol 13, 759188. [PubMed: 35126389]

Goswami S, Anandhan S, Raychaudhuri D, and Sharma P (2022). Myeloid cell-targeted therapies for solid tumours. Nat Rev Immunol.

Habermann AC, Gutierrez AJ, Bui LT, Yahn SL, Winters NI, Calvi CL, Peter L, Chung MI, Taylor CJ, Jetter C, et al. (2020). Single-cell RNA sequencing reveals profibrotic roles of distinct epithelial and mesenchymal lineages in pulmonary fibrosis. Sci Adv 6, eaba1972. [PubMed: 32832598]

Hamy AS, Tury S, Wang X, Gao J, Pierga JY, Giacchetti S, Brain E, Pistilli B, Marty M, Espie M, et al. (2019). Celecoxib With Neoadjuvant Chemotherapy for Breast Cancer Might Worsen Outcomes Differentially by COX-2 Expression and ER Status: Exploratory Analysis of the REMAGUS02 Trial. J Clin Oncol 37, 624–635. [PubMed: 30702971]

Hawk E, Maresso KC, and Brown P (2018). NSAIDs to Prevent Breast Cancer Recurrence? An Unanswered Question. Journal of the National Cancer Institute 110, 927–928. [PubMed: 29554350]

Headley MB, Bins A, Nip A, Roberts EW, Looney MR, Gerard A, and Krummel MF (2016). Visualization of immediate immune responses to pioneer metastatic cells in the lung. Nature 531, 513–517. [PubMed: 26982733]

Helft J, Bottcher J, Chakravarty P, Zelenay S, Huotari J, Schraml BU, Goubau D, and Reis e Sousa C (2015). GM-CSF Mouse Bone Marrow Cultures Comprise a Heterogeneous Population of CD11c(+)MHCII(+) Macrophages and Dendritic Cells. Immunity 42, 1197–1211. [PubMed: 26084029]

Holland CH, Tanevski J, Perales-Paton J, Gleixner J, Kumar MP, Mereu E, Joughin BA, Stegle O, Lauffenburger DA, Heyn H, et al. (2020). Robustness and applicability of transcription factor and pathway analysis tools on single-cell RNA-seq data. Genome Biol 21, 36. [PubMed: 32051003]

Iams WT, Porter J, and Horn L (2020). Immunotherapeutic approaches for small-cell lung cancer. Nat Rev Clin Oncol 17, 300–312. [PubMed: 32055013]

Ishikawa TO, Jain NK, Taketo MM, and Herschman HR (2006). Imaging cyclooxygenase-2 (Cox-2) gene expression in living animals with a luciferase knock-in reporter gene. Mol Imaging Biol 8, 171–187. [PubMed: 16557423]

Kaplan RN, Riba RD, Zacharoulis S, Bramley AH, Vincent L, Costa C, MacDonald DD, Jin DK, Shido K, Kerns SA, et al. (2005). VEGFR1-positive haematopoietic bone marrow progenitors initiate the pre-metastatic niche. Nature 438, 820–827. [PubMed: 16341007]

King EM, Kaur M, Gong W, Rider CF, Holden NS, and Newton R (2009). Regulation of tristetraprolin expression by interleukin-1 beta and dexamethasone in human pulmonary epithelial cells: roles for nuclear factor-kappa B and p38 mitogen-activated protein kinase. J Pharmacol Exp Ther 330, 575–585. [PubMed: 19435930]

Kitamura T, Qian BZ, and Pollard JW (2015). Immune cell promotion of metastasis. Nat Rev Immunol 15, 73–86. [PubMed: 25614318]

Kolahian S, Fernandez IE, Eickelberg O, and Hartl D (2016). Immune Mechanisms in Pulmonary Fibrosis. Am J Respir Cell Mol Biol 55, 309–322. [PubMed: 27149613]

Koliaraki V, Prados A, Armaka M, and Kollias G (2020). The mesenchymal context in inflammation, immunity and cancer. Nat Immunol 21, 974–982. [PubMed: 32747813]

Krausgruber T, Fortelny N, Fife-Gernedl V, Senekowitsch M, Schuster LC, Lercher A, Nemc A, Schmidl C, Rendeiro AF, Bergthaler A, and Bock C (2020). Structural cells are key regulators of organ-specific immune responses. Nature 583, 296–302. [PubMed: 32612232]

Lambert AW, Pattabiraman DR, and Weinberg RA (2017). Emerging Biological Principles of Metastasis. Cell 168, 670–691. [PubMed: 28187288]

Le Naour A, Koffi Y, Diab M, Le Guennec D, Rouge S, Aldekwer S, Goncalves-Mendes N, Talvas J, Farges MC, Caldefie-Chezet F, et al. (2020). EO771, the first luminal B mammary cancer cell line from C57BL/6 mice. Cancer Cell Int 20, 328. [PubMed: 32699527]

Li P, Lu M, Shi J, Gong Z, Hua L, Li Q, Lim B, Zhang XH, Chen X, Li S, et al. (2020a). Lung mesenchymal cells elicit lipid storage in neutrophils that fuel breast cancer lung metastasis. Nat Immunol 21, 1444–1455. [PubMed: 32958928]

Li P, Lu M, Shi J, Hua L, Gong Z, Li Q, Shultz LD, and Ren G (2020b). Dual roles of neutrophils in metastatic colonization are governed by the host NK cell status. Nat Commun 11, 4387. [PubMed: 32873795]

Liu Y, and Cao X (2016). Characteristics and Significance of the Pre-metastatic Niche. Cancer cell 30, 668–681. [PubMed: 27846389]

Lopez-Soto A, Gonzalez S, Smyth MJ, and Galluzzi L (2017). Control of Metastasis by NK Cells. Cancer Cell 32, 135–154. [PubMed: 28810142]

Lu W, Yu W, He J, Liu W, Yang J, Lin X, Zhang Y, Wang X, Jiang W, Luo J, et al. (2021). Reprogramming immunosuppressive myeloid cells facilitates immunotherapy for colorectal cancer. EMBO Mol Med 13, e12798. [PubMed: 33283987]

Lutz MB, Strobl H, Schuler G, and Romani N (2017). GM-CSF Monocyte-Derived Cells and Langerhans Cells As Part of the Dendritic Cell Family. Front Immunol 8, 1388. [PubMed: 29109731]

Mackay CR (2001). Chemokines: immunology's high impact factors. Nat Immunol 2, 95–101. [PubMed: 11175800]

Massague J, and Obenauf AC (2016). Metastatic colonization by circulating tumour cells. Nature 529, 298–306. [PubMed: 26791720]

Mazhar D, Ang R, and Waxman J (2006). COX inhibitors and breast cancer. British journal of cancer 94, 346–350. [PubMed: 16421592]

Misharin AV, Morales-Nebreda L, Mutlu GM, Budinger GR, and Perlman H (2013). Flow cytometric analysis of macrophages and dendritic cell subsets in the mouse lung. Am J Respir Cell Mol Biol 49, 503–510. [PubMed: 23672262]

Mittal M, Tiruppathi C, Nepal S, Zhao YY, Grzych D, Soni D, Prockop DJ, and Malik AB (2016). TNFalpha-stimulated gene-6 (TSG6) activates macrophage phenotype transition to prevent inflammatory lung injury. Proc Natl Acad Sci U S A 113, E8151–E8158. [PubMed: 27911817]

Miura A, Shimbo T, Kitayama T, Ouchi Y, Yamazaki S, Nishida M, Takaki E, Yamamoto R, Wijaya E, and Tamai K (2021). Contribution of PDGFRalpha lineage cells in adult mouse hematopoiesis. Biochem Biophys Res Commun 534, 186–192. [PubMed: 33309273]

Mizgerd JP (2012). Respiratory infection and the impact of pulmonary immunity on lung health and disease. Am J Respir Crit Care Med 186, 824–829. [PubMed: 22798317]

Nakanishi M, and Rosenberg DW (2013). Multifaceted roles of PGE2 in inflammation and cancer. Semin Immunopathol 35, 123–137. [PubMed: 22996682]

Neyt K, and Lambrecht BN (2013). The role of lung dendritic cell subsets in immunity to respiratory viruses. Immunol Rev 255, 57–67. [PubMed: 23947347]

Palucka K, and Banchereau J (2013). Dendritic-cell-based therapeutic cancer vaccines. Immunity 39, 38–48. [PubMed: 23890062]

Pannunzio A, and Coluccia M (2018). Cyclooxygenase-1 (COX-1) and COX-1 Inhibitors in Cancer: A Review of Oncology and Medicinal Chemistry Literature. Pharmaceuticals 11.

Pathria P, Louis TL, and Varner JA (2019). Targeting Tumor-Associated Macrophages in Cancer. Trends Immunol 40, 310–327. [PubMed: 30890304]

Peinado H, Zhang H, Matei IR, Costa-Silva B, Hoshino A, Rodrigues G, Psaila B, Kaplan RN, Bromberg JF, Kang Y, et al. (2017). Pre-metastatic niches: organ-specific homes for metastases. Nat Rev Cancer 17, 302–317. [PubMed: 28303905]

Peng S, Hu P, Xiao YT, Lu W, Guo D, Hu S, Xie J, Wang M, Yu W, Yang J, et al. (2022). Single-Cell Analysis Reveals EP4 as a Target for Restoring T-Cell Infiltration and Sensitizing Prostate Cancer to Immunotherapy. Clin Cancer Res 28, 552–567. [PubMed: 34740924]

Perruche S, Zhang P, Liu Y, Saas P, Bluestone JA, and Chen W (2008). CD3-specific antibody-induced immune tolerance involves transforming growth factor-beta from phagocytes digesting apoptotic T cells. Nat Med 14, 528–535. [PubMed: 18438416]

Pulaski BA, and Ostrand-Rosenberg S (2001). Mouse 4T1 breast tumor model. Curr Protoc Immunol *Chapter 20*, Unit 20 22.

Qian BZ, Li J, Zhang H, Kitamura T, Zhang J, Campion LR, Kaiser EA, Snyder LA, and Pollard JW (2011). CCL2 recruits inflammatory monocytes to facilitate breast-tumour metastasis. Nature 475, 222–225. [PubMed: 21654748]

Reader J, Holt D, and Fulton A (2011). Prostaglandin E2 EP receptors as therapeutic targets in breast cancer. Cancer metastasis reviews 30, 449–463. [PubMed: 22002714]

Regulski M, Regulska K, Prukala W, Piotrowska H, Stanisz B, and Murias M (2016). COX-2 inhibitors: a novel strategy in the management of breast cancer. Drug discovery today 21, 598–615. [PubMed: 26723915]

Rhodes DR, Yu J, Shanker K, Deshpande N, Varambally R, Ghosh D, Barrette T, Pandey A, and Chinnaiyan AM (2004). ONCOMINE: a cancer microarray database and integrated data-mining platform. Neoplasia 6, 1–6. [PubMed: 15068665]

Ritchie ME, Phipson B, Wu D, Hu Y, Law CW, Shi W, and Smyth GK (2015). limma powers differential expression analyses for RNA-sequencing and microarray studies. Nucleic Acids Res 43, e47. [PubMed: 25605792]

Roth RB, Hevezi P, Lee J, Willhite D, Lechner SM, Foster AC, and Zlotnik A (2006). Gene expression analyses reveal molecular relationships among 20 regions of the human CNS. Neurogenetics 7, 67–80. [PubMed: 16572319]

Sajiki Y, Konnai S, Cai Z, Takada K, Okagawa T, Maekawa N, Fujisawa S, Kato Y, Suzuki Y, Murata S, and Ohashi K (2020). Enhanced Immunotherapeutic Efficacy of Anti-PD-L1 Antibody in Combination with an EP4 Antagonist. Immunohorizons 4, 837–850. [PubMed: 33443026]

Saleh R, and Elkord E (2020). Acquired resistance to cancer immunotherapy: Role of tumor-mediated immunosuppression. Semin Cancer Biol 65, 13–27. [PubMed: 31362073]

Samad TA, Moore KA, Sapirstein A, Billet S, Allchorne A, Poole S, Bonventre JV, and Woolf CJ (2001). Interleukin-1beta-mediated induction of Cox-2 in the CNS contributes to inflammatory pain hypersensitivity. Nature 410, 471–475. [PubMed: 11260714]

Samarelli AV, Tonelli R, Heijink I, Martin Medina A, Marchioni A, Bruzzi G, Castaniere I, Andrisani D, Gozzi F, Manicardi L, et al. (2021). Dissecting the Role of Mesenchymal Stem Cells in Idiopathic Pulmonary Fibrosis: Cause or Solution. Front Pharmacol 12, 692551. [PubMed: 34290610]

Sanduja S, Blanco FF, Young LE, Kaza V, and Dixon DA (2012). The role of tristetraprolin in cancer and inflammation. Front Biosci (Landmark Ed) 17, 174–188. [PubMed: 22201737]

Sharma P, and Allison JP (2015). The future of immune checkpoint therapy. Science 348, 56–61. [PubMed: 25838373]

Siiskonen H, Oikari S, Pasonen-Seppanen S, and Rilla K (2015). Hyaluronan synthase 1: a mysterious enzyme with unexpected functions. Front Immunol 6, 43. [PubMed: 25699059]

Spiegel A, Brooks MW, Houshyar S, Reinhardt F, Ardolino M, Fessler E, Chen MB, Krall JA, DeCock J, Zervantonakis IK, et al. (2016). Neutrophils Suppress Intraluminal NK Cell-Mediated Tumor Cell Clearance and Enhance Extravasation of Disseminated Carcinoma Cells. Cancer discovery 6, 630–649. [PubMed: 27072748]

Stenmark KR, Nozik-Grayck E, Gerasimovskaya E, Anwar A, Li M, Riddle S, and Frid M (2011). The adventitia: Essential role in pulmonary vascular remodeling. Compr Physiol 1, 141–161. [PubMed: 23737168]

Stewart TJ, and Abrams SI (2007). Altered immune function during long-term host-tumor interactions can be modulated to retard autochthonous neoplastic growth. J Immunol 179, 2851–2859. [PubMed: 17709499]

Strasser-Weippl K, Higgins MJ, Chapman JW, Ingle JN, Sledge GW, Budd GT, Ellis MJ, Pritchard KI, Clemons MJ, Badovinac-Crnjevic T, et al. (2018). Effects of Celecoxib and Low-dose Aspirin on Outcomes in Adjuvant Aromatase Inhibitor-Treated Patients: CCTG MA.27. Journal of the National Cancer Institute 110, 1003–1008. [PubMed: 29554282]

Stuart T, Butler A, Hoffman P, Hafemeister C, Papalexi E, Mauck WM 3rd, Hao Y, Stoeckius M, Smibert P, and Satija R (2019). Comprehensive Integration of Single-Cell Data. Cell 177, 1888–1902 e1821. [PubMed: 31178118]

Subramanian Vignesh K, and Deepe GS Jr. (2017). Metallothioneins: Emerging Modulators in Immunity and Infection. Int J Mol Sci 18.

Tanaka T, Narazaki M, and Kishimoto T (2014). IL-6 in inflammation, immunity, and disease. Cold Spring Harb Perspect Biol 6, a016295. [PubMed: 25190079]

Taniguchi K, and Karin M (2018). NF-kappaB, inflammation, immunity and cancer: coming of age. Nat Rev Immunol 18, 309–324. [PubMed: 29379212]

Tokumasu M, Nishida M, Kawaguchi T, Kudo I, Kotani T, Takeda K, Yoshida T, and Udono H (2022). Blocking EP4 downregulates tumor metabolism and synergizes with anti-PD-1 therapy to activate natural killer cells in a lung adenocarcinoma model. Int Immunol.

Travaglini KJ, Nabhan AN, Penland L, Sinha R, Gillich A, Sit RV, Chang S, Conley SD, Mori Y, Seita J, et al. (2020). A molecular cell atlas of the human lung from single-cell RNA sequencing. Nature 587, 619–625. [PubMed: 33208946]

Ushakumary MG, Riccetti M, and Perl AT (2021). Resident interstitial lung fibroblasts and their role in alveolar stem cell niche development, homeostasis, injury, and regeneration. Stem Cells Transl Med 10, 1021–1032. [PubMed: 33624948]

Vermaelen K, and Pauwels R (2005). Pulmonary dendritic cells. Am J Respir Crit Care Med 172, 530–551. [PubMed: 15879415]

Vesely MD, Kershaw MH, Schreiber RD, and Smyth MJ (2011). Natural innate and adaptive immunity to cancer. Annu Rev Immunol 29, 235–271. [PubMed: 21219185]

Wang L, Li Z, Ciric B, Safavi F, Zhang GX, and Rostami A (2016). Selective depletion of CD11c(+) CD11b(+) dendritic cells partially abrogates tolerogenic effects of intravenous MOG in murine EAE. Eur J Immunol 46, 2454–2466. [PubMed: 27338697]

Wang Y, Cui L, Georgiev P, Singh L, Zheng Y, Yu Y, Grein J, Zhang C, Muise ES, Sloman DL, et al. (2021). Combination of EP4 antagonist MF-766 and anti-PD-1 promotes anti-tumor efficacy by modulating both lymphocytes and myeloid cells. Oncoimmunology 10, 1896643. [PubMed: 33796403]

Wculek SK, Cueto FJ, Mujal AM, Melero I, Krummel MF, and Sancho D (2020). Dendritic cells in cancer immunology and immunotherapy. Nat Rev Immunol 20, 7–24. [PubMed: 31467405]

Wen AY, Sakamoto KM, and Miller LS (2010). The role of the transcription factor CREB in immune function. J Immunol 185, 6413–6419. [PubMed: 21084670]

Xie T, Wang Y, Deng N, Huang G, Taghavifar F, Geng Y, Liu N, Kulur V, Yao C, Chen P, et al. (2018). Single-Cell Deconvolution of Fibroblast Heterogeneity in Mouse Pulmonary Fibrosis. Cell Rep 22, 3625–3640. [PubMed: 29590628]

Yu H, Pardoll D, and Jove R (2009). STATs in cancer inflammation and immunity: a leading role for STAT3. Nat Rev Cancer 9, 798–809. [PubMed: 19851315]

Zepp JA, Zacharias WJ, Frank DB, Cavanaugh CA, Zhou S, Morley MP, and Morrisey EE (2017). Distinct Mesenchymal Lineages and Niches Promote Epithelial Self-Renewal and Myofibrogenesis in the Lung. Cell 170, 1134–1148 e1110. [PubMed: 28886382]

Zhou Y, Zhou B, Pache L, Chang M, Khodabakhshi AH, Tanaseichuk O, Benner C, and Chanda SK (2019). Metascape provides a biologist-oriented resource for the analysis of systems-level datasets. Nat Commun 10, 1523. [PubMed: 30944313]

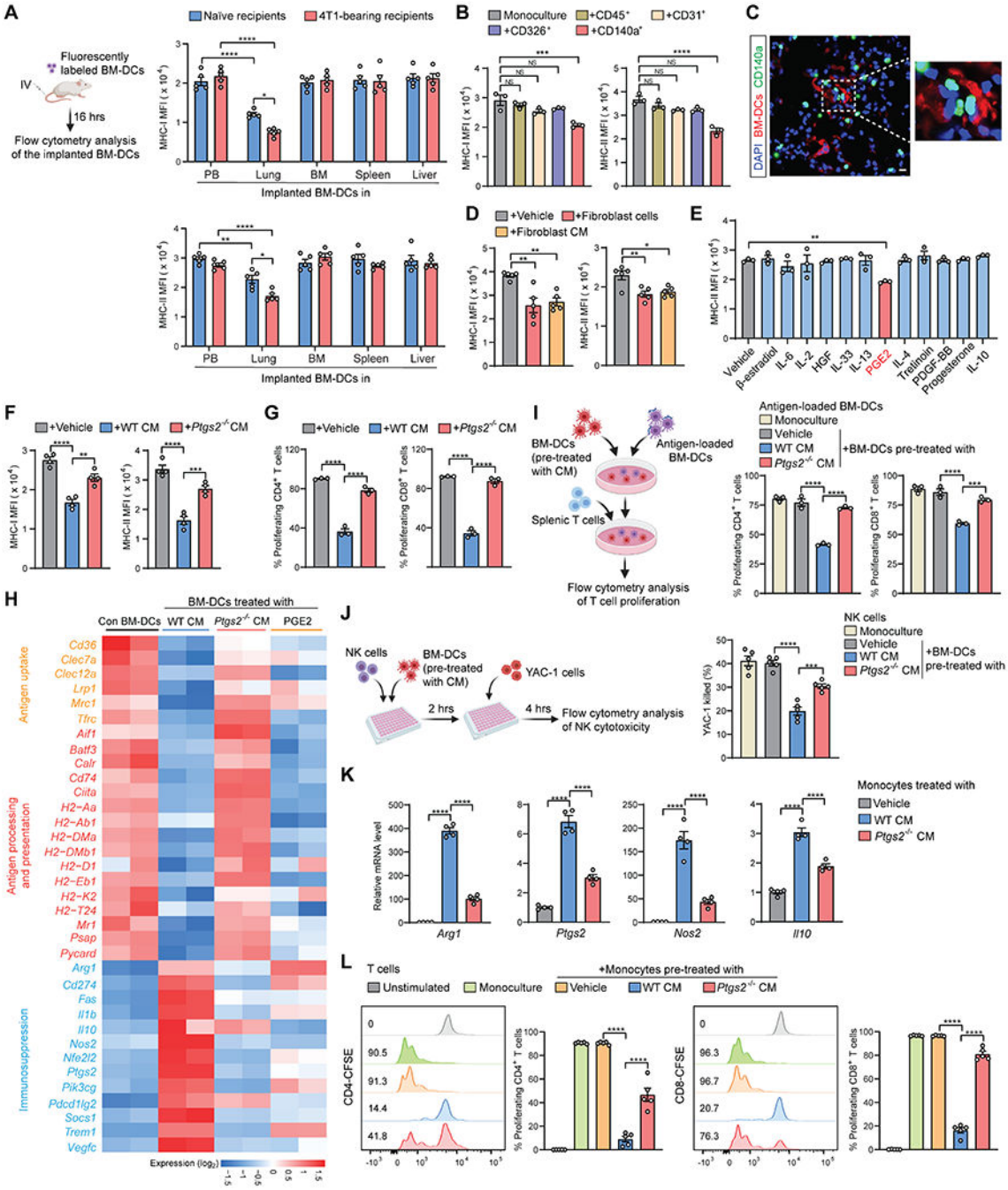

Figure 1. Lung fibroblasts reprogram BM-DCs and monocytes to be dysfunctional or immunosuppressive via COX-2

(**A**) MHC-I and MHC-II expression of implanted BM-DCs in different tissues and organs was measured after transfer into naïve or 4T1 tumor-bearing mice (n=5). MFI, mean fluorescence intensity.

(**B**) MHC-I and MHC-II expression of BM-DCs was measured after monoculture or co-culture with the indicated lung tissue cells isolated from naïve mice (n=3).

(**C**) Localization of implanted BM-DCs and resident CD140a^{+} fibroblasts in lung section of naïve *CD140a*^{EGFP} mouse. Scale bar, 10 μm.
(**D**) MHC-I and MHC-II expression of BM-DCs was measured after co-culture with CD140a^{+} lung fibroblasts or fibroblast-derived CM (n=5).
(**E**) MHC-II expression of BM-DCs was measured after stimulation with the indicated factors (n=3).
(**F** and **G**) MHC-I and MHC-II expression (**F**) and T cell priming capacities (**G**) of BM-DCs were measured after stimulation with WT or *Ptgs2*$^{-/-}$ lung fibroblast CM (n=3-4).
(**H**) Heatmap showing the expression of selected genes from the RNA-seq data of BM-DCs.
(**I**-**J**) Effect of BM-DCs on proliferation of T cells (**I**) or cytotoxicity of NK cells (**J**) was analyzed after stimulation with WT or *Ptgs2*$^{-/-}$ lung fibroblast CM (n=3-5).
(**K**-**L**) Expression of indicated genes (**K**) and effect on T cell proliferation (**L**) of BM-derived monocytes was measured after stimulation with WT or *Ptgs2*$^{-/-}$ lung fibroblast CM (n=4-5).
n is the number of biological replicates. Data are representative of at least five independent experiments (**A**-**G**, **I**-**L**) and shown as mean ± SEM. *p< 0.05, **p< 0.01, ***p< 0.001; ****p< 0.0001; NS, not significant, by one-way ANOVA (**B**, **D**-**G**, **I**-**L**) or two-way ANOVA (**A**). See also Figure S1.

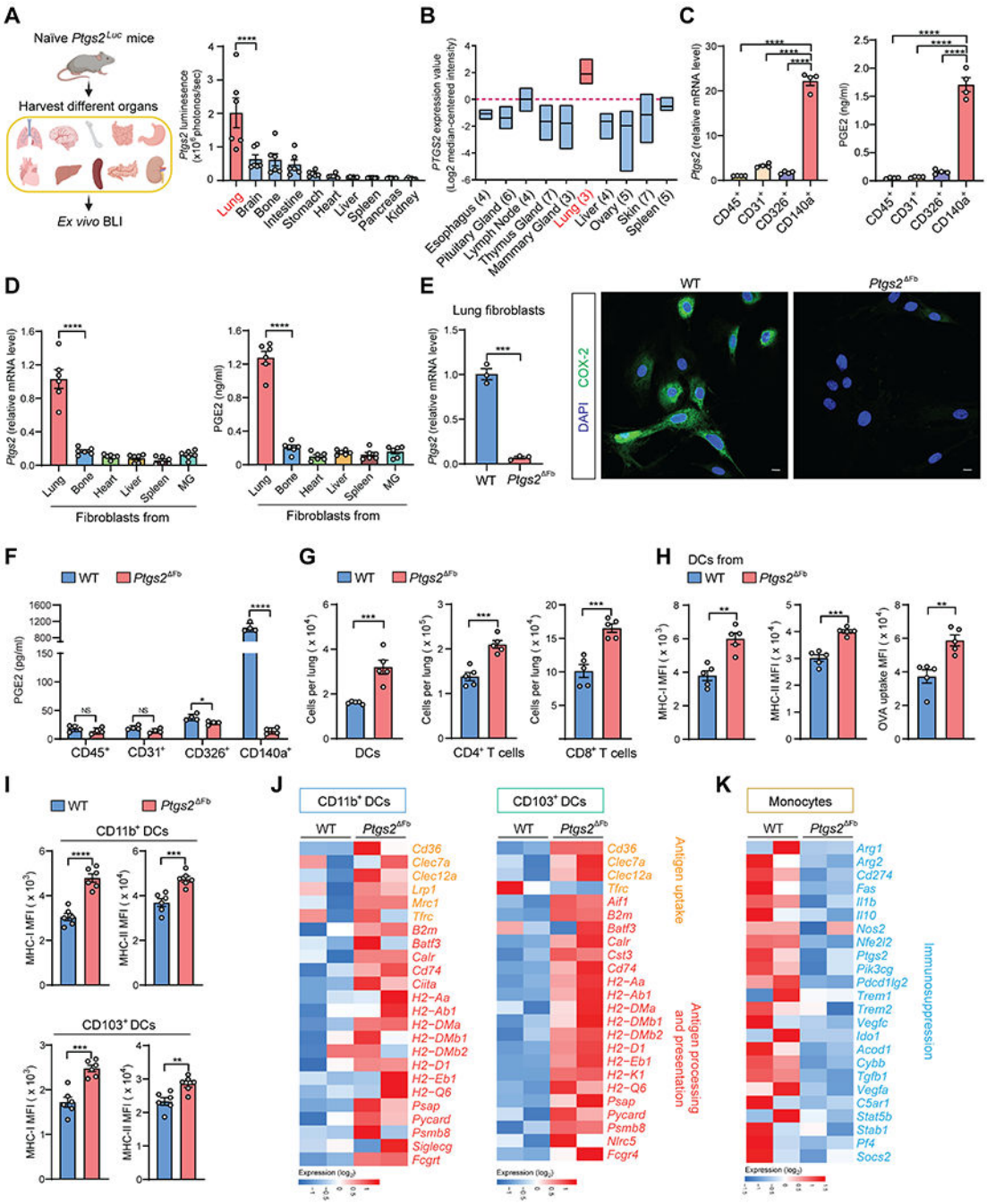

Figure 2. *Ptgs2*-expressing lung fibroblasts modulate the lung resident immune microenvironment at the steady state

(**A**) Quantification of *Ptgs2* expression in different organs isolated from naïve *Ptgs2*^{Luc} mice (n=6).

(**B**) Analysis of *PTGS2* expression in human normal tissue microarray data (GSE7307).

(**C-D**) *Ptgs2* expression and PGE2 production was measured in the indicated lung tissue cells (**C**) or different tissue-derived fibroblasts (**D**) isolated from naïve mice (n=4-6). MG, mammary gland.

(**E**) *Ptgs2* expression (*left*) and COX-2 protein level (*right*) was detected in lung CD140a$^+$ fibroblasts from WT or *Ptgs2*$^{\Delta Fb}$ naïve mice. Scale bars, 10 μm.

(**F-G**) PGE2 production of indicated lung tissue cells (**F**) and the total number of lung DCs, CD4$^+$ and CD8$^+$ T cells (**G**) was measured in WT or *Ptgs2*$^{\Delta Fb}$ naïve mice (n=4-5).

(**H**) MHC-I and MHC-II expression and OVA uptake ability was determined in lung DCs from WT or *Ptgs2*$^{\Delta Fb}$ naïve mice (n=5).

(I) MHC-I and MHC-II expression was determined in lung CD11b$^+$ and CD103$^+$ DCs from WT or *Ptgs2*$^{\Delta Fb}$ naïve mice (n=6).

(**J** and **K**) Heatmap showing expression of indicated genes from the RNA-seq data of lung CD11b$^+$ or CD103$^+$ DCs (**J**) and conventional monocytes (**K**) from WT or *Ptgs2*$^{\Delta Fb}$ naïve mice.

n is the number of biological replicates. Data are representative of at least three (**A**, **D**, **I**) or five (**C**, **E-H**) independent experiments and shown as mean ± SEM. *p< 0.05, **p< 0.01, ***p< 0.001; ****p< 0.0001; NS, not significant, by one-way ANOVA (**A**, **C-D**) or unpaired Student's t-test (**E-I**). See also Figure S2.

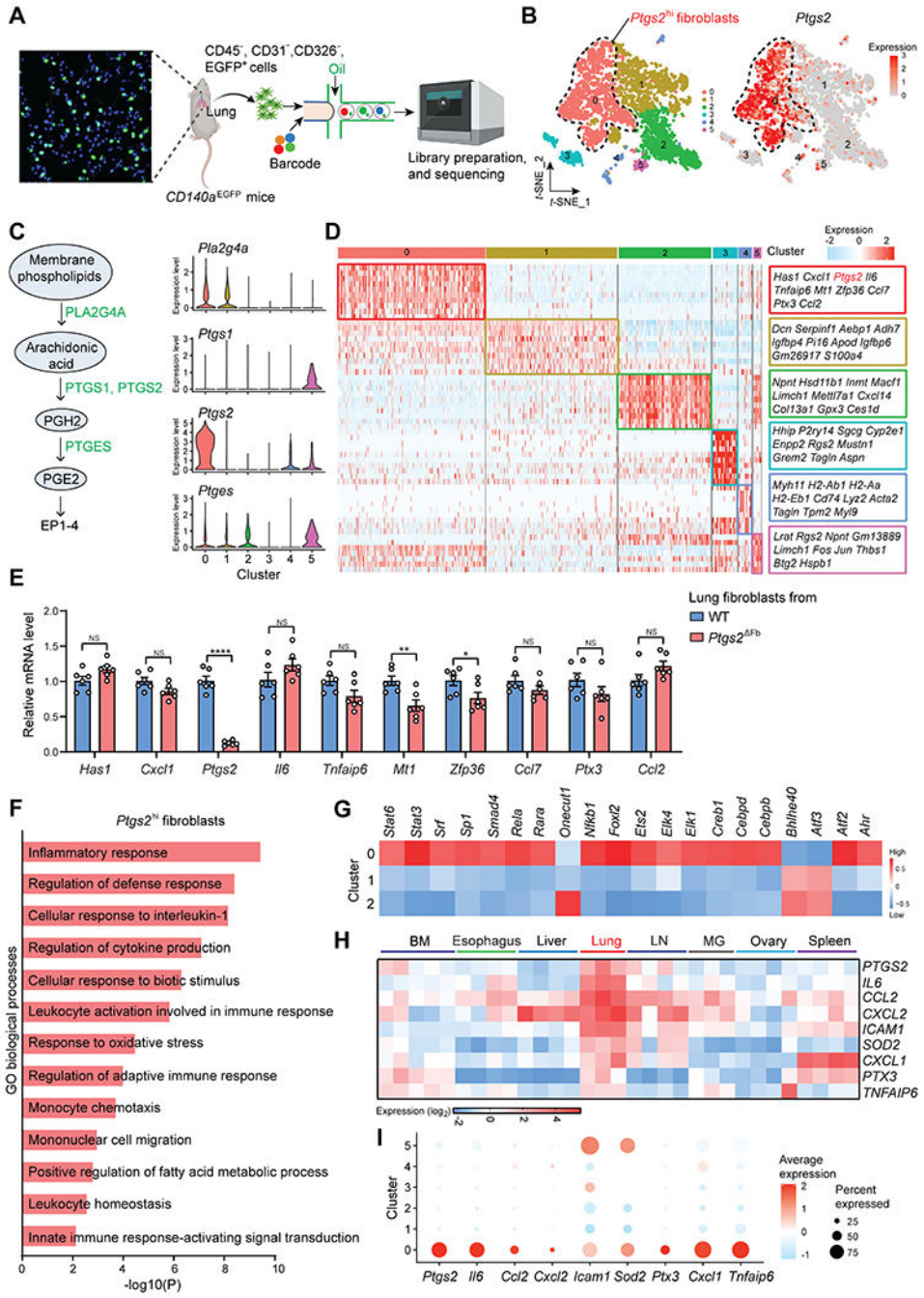

Figure 3. Identification of *Ptgs2*-expressing fibroblasts by scRNA-seq

(**A**) Workflow depicts isolation of CD140a^{+} lung fibroblasts from naïve *CD140a*^{EGFP} mice for scRNA-seq.

(**B**) t-SNE plots (*left*) and feature plots (*right*) showing the *Ptgs2*^{hi} fibroblasts (cluster 0) among lung CD140a^{+} fibroblasts.

(**C**) Schematic showing the PGE2 synthesis pathway (*left*), and violin plots (*right*) showing the expression levels of the indicated genes across each cluster.

(**D**) Heatmap showing the expression of the top-rated marker genes across each cluster.

(**E**) mRNA expression of the indicated genes was measured in lung fibroblasts isolated from WT or *Ptgs2*$^{\Delta Fb}$ naïve mice (n=6).
(**F**) Enrichment analysis for Gene Ontology terms in *Ptgs2*^{hi} fibroblasts (cluster 0).
(**G**) Heatmap showing transcription factor activity analysis of the three major fibroblast subsets (clusters 0, 1 and 2).
(**H**) Heatmap showing co-expression analysis of human genes co-expressed with *PTGS2* from human normal tissue microarray data (GSE3526). LN, lymph node.
(**I**) Dot plots showing expression of the selected genes across each cluster.
n is the number of biological replicates. Data are representative of at least three independent experiments (**E**). *p< 0.05, **p< 0.01, ****p< 0.0001; NS, not significant, by unpaired Student's t-test (**E**). See also Figure S3.

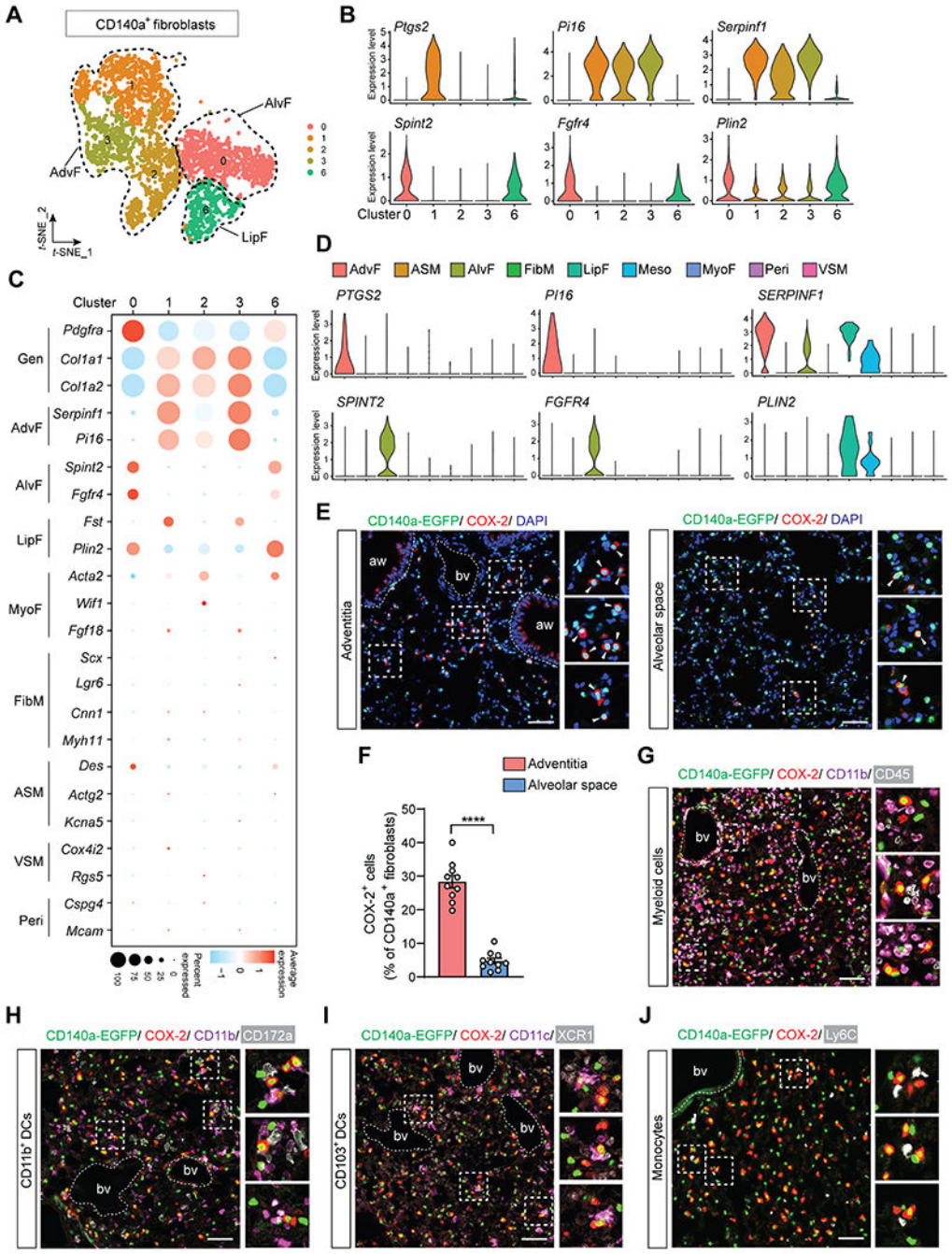

Figure 4. *Ptgs2*^{hi} lung fibroblasts localize primarily within the lung adventitial space

(**A**) t-SNE plots showing lung CD140a^{+} fibroblasts from the scRNA-seq data in Figure S3A. AdvF, adventitial fibroblast; AlvF, alveolar fibroblast; LipF, lipofibroblast.

(**B** and **C**) Violin plots (**B**) and dot plots (**C**) showing expression of the indicated genes across each cluster. Gen, general fibroblast; MyoF, myofibroblast; FibM, fibromyocyte; ASM, airway smooth muscle; VSM, vascular smooth muscle; Peri, pericyte.

(**D**) Violin plots showing expression of the indicated genes in human lung stromal cells from a published dataset (EGAS00001004344). Meso, mesothelial cells.

(**E** and **F**) Representative images showing the localization of CD140a-GFP$^+$ COX-2$^+$ cells in naïve mouse lung adventitia or alveolar space (**E**), and the percentage of COX-2$^+$ cells among CD140a$^+$ fibroblasts was quantified in these two regions (**F**). For the percentage calculation, two pictures were chosen for each region from each mouse lung section; n = 5 mice per group. Scale bars, 50 μm. aw, airway; bv, blood vessel.

(**G-J**) Representative images showing the localization of CD140a-GFP$^+$ COX-2$^+$ cells and myeloid cells (**G**), CD11b$^+$ DCs (**H**), CD103$^+$ DCs (**I**), or conventional monocytes (**J**) in pre-metastatic lung sections of AT3 tumor-bearing mice. Scale bars, 50 μm.

n is the number of biological replicates. Data are representative of at least three independent experiments (**E-J**). ****p< 0.0001, by unpaired Student's t-test (**F**).

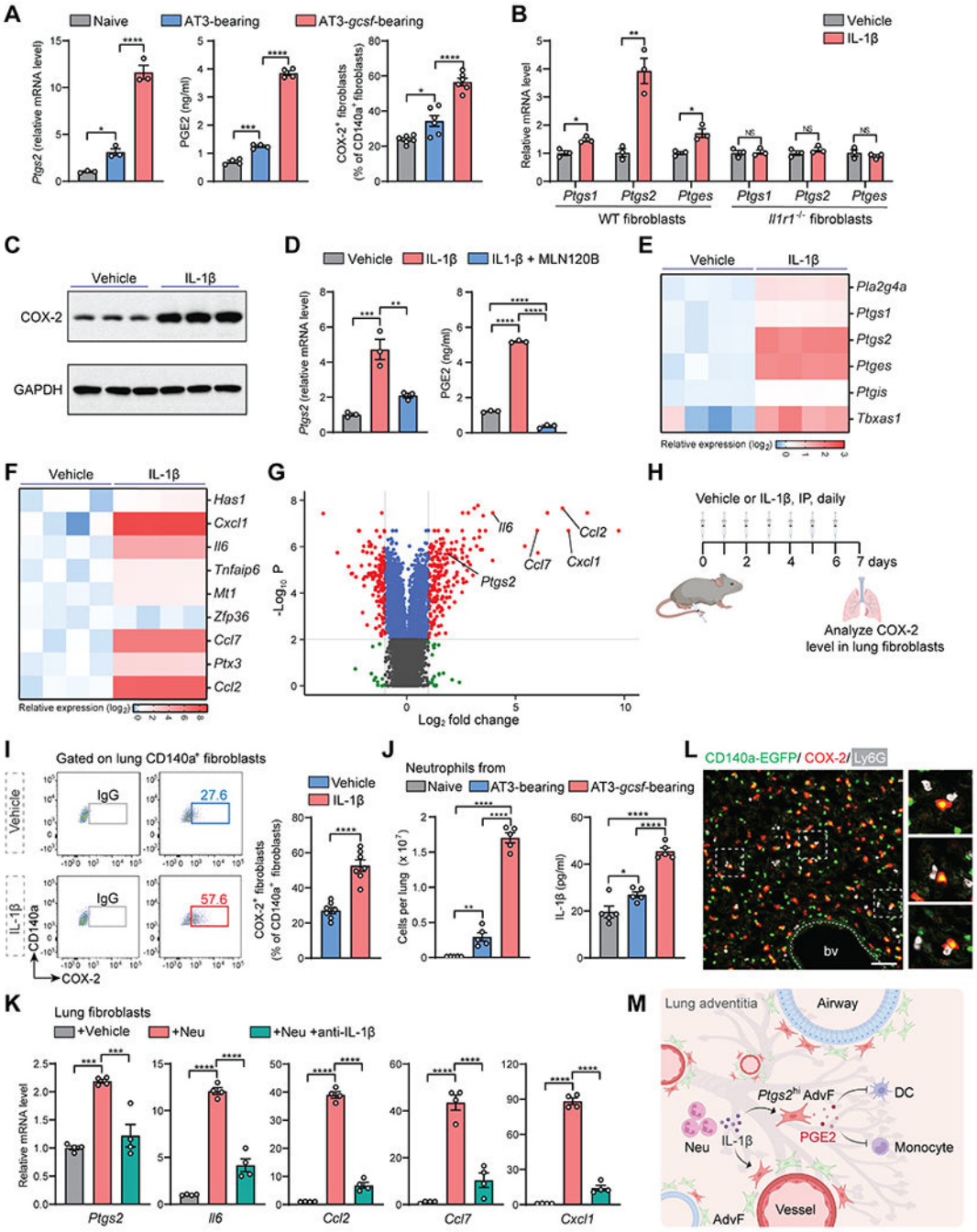

Figure 5. IL-1β reinforces the phenotype of *Ptgs2*^{hi} lung fibroblasts

(**A**) *Ptgs2* expression (*left*), PGE2 production (*middle*), and frequency of COX-2^{+} cells (*right*) was measured in lung CD140a^{+} fibroblasts from naïve, AT3 and AT3-*gcsf* tumor-bearing mice (n=3-6).

(**B**) Expression of the indicated genes in *ex vivo* cultured WT and *Il1r*$^{-/-}$ lung fibroblasts upon stimulation by vehicle or IL-1β (n=3).

(**C**) COX-2 protein level in *ex vivo* cultured naïve mouse-derived lung fibroblasts stimulated with vehicle or IL-1β.

(**D**) *Ptgs2* expression (*left*) and PGE2 production (*right*) was measured in lung CD140a^{+} fibroblasts after stimulation with IL-1β in the absence or presence of NFκB pathway inhibitor MLN120B (n=3).

(**E** and **F**) Heatmap showing expression of the indicated genes in the RNA-seq data of lung fibroblasts.

(**G**) Volcano plots showing fold change and P-value for the comparison of IL-1β-treated and vehicle-treated lung fibroblasts based on the RNA-seq data.

(**H** and **I**) As depicted in the schematic (**H**), the frequency of COX-2^{+} fibroblasts was measured among lung CD140a^{+} fibroblasts upon treatment by IL-1β (**I**) (n=7). Negative control IgG is shown.

(**J**) Cell number (*left*) and IL-1β production (*right*) of lung neutrophils was quantified in naïve, AT3 and AT3-*gcsf* tumor-bearing mice (n=5).

(**K**) Expression of the indicated genes was measured in lung fibroblasts after co-culture with lung neutrophils isolated from AT3-*gcsf* tumor-bearing mice in the absence or presence of anti-IL-1β (n=4).

(**L**) Representative images showing the localization of CD140a-GFP^{+} COX-2^{+} cells and neutrophils in pre-metastatic lung sections. Scale bar, 50 μm.

(**M**) Schematic showing that the immunoregulatory program by *Ptgs2*^{hi} lung AdvF can be reinforced by IL-1β.

n is the number of biological replicates. Data are representative of at least five independent experiments (**A-D**, **I-L**) and shown as mean ± SEM. *p< 0.05, **p< 0.01, ***p< 0.001; ****p< 0.0001; NS, not significant, by one-way ANOVA (**A**, **D**, **J-K**) or unpaired Student's t-test (**B**, **I**). See also Figure S4.

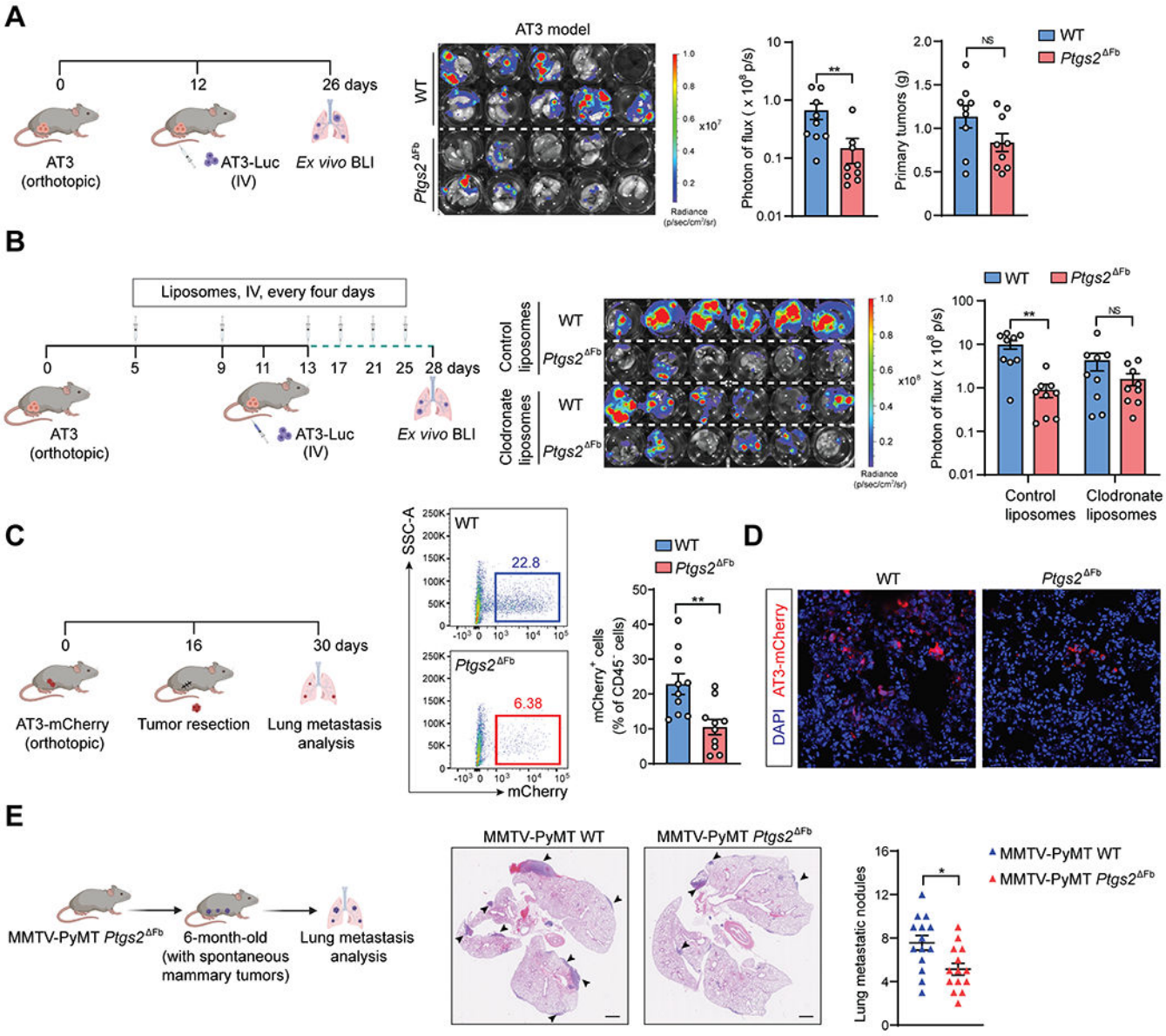

Figure 6. Genetic ablation of *Ptgs2* in CD140a^{+} fibroblasts mitigates lung metastasis of breast cancer

(**A**) As depicted in the schematic (*left*), lung metastatic colonization in WT or *Ptgs2*$^{\Delta Fb}$ recipient mice was measured by *ex vivo* bioluminescent imaging (BLI). The primary tumor weight was also compared between the two recipient mice (n=9).

(**B**) As depicted in the schematic (*left*), lung metastatic colonization was determined in WT or *Ptgs2*$^{\Delta Fb}$ mice treated with control or clodronate liposomes (n=9).

(**C** and **D**) As depicted in the schematic (*left*), the percentage of AT3-mCherry cells was measured in WT or *Ptgs2*$^{\Delta Fb}$ mice (**C**) (n=10). Representative images were taken from (**C**) to show mCherry^{+} AT3 cells in lung sections (**D**). Scale bars, 25 μm.

(**E**) Comparison of spontaneous lung metastases occurring in MMTV-PyMT *Ptgs2*$^{\Delta Fb}$ mice and their WT littermates (n=14). Representative histological lung sections stained with H&E are shown and arrowheads indicate metastatic lesions. Scale bars, 1mm.

n is the number of biological replicates. Data are representative of at least two independent experiments (**A-C, E**) and shown as mean ± SEM. *p< 0.05, **p< 0.01; NS, not significant, by Mann-Whitney test (**A-C, E**). See also Figures S5 and S6.

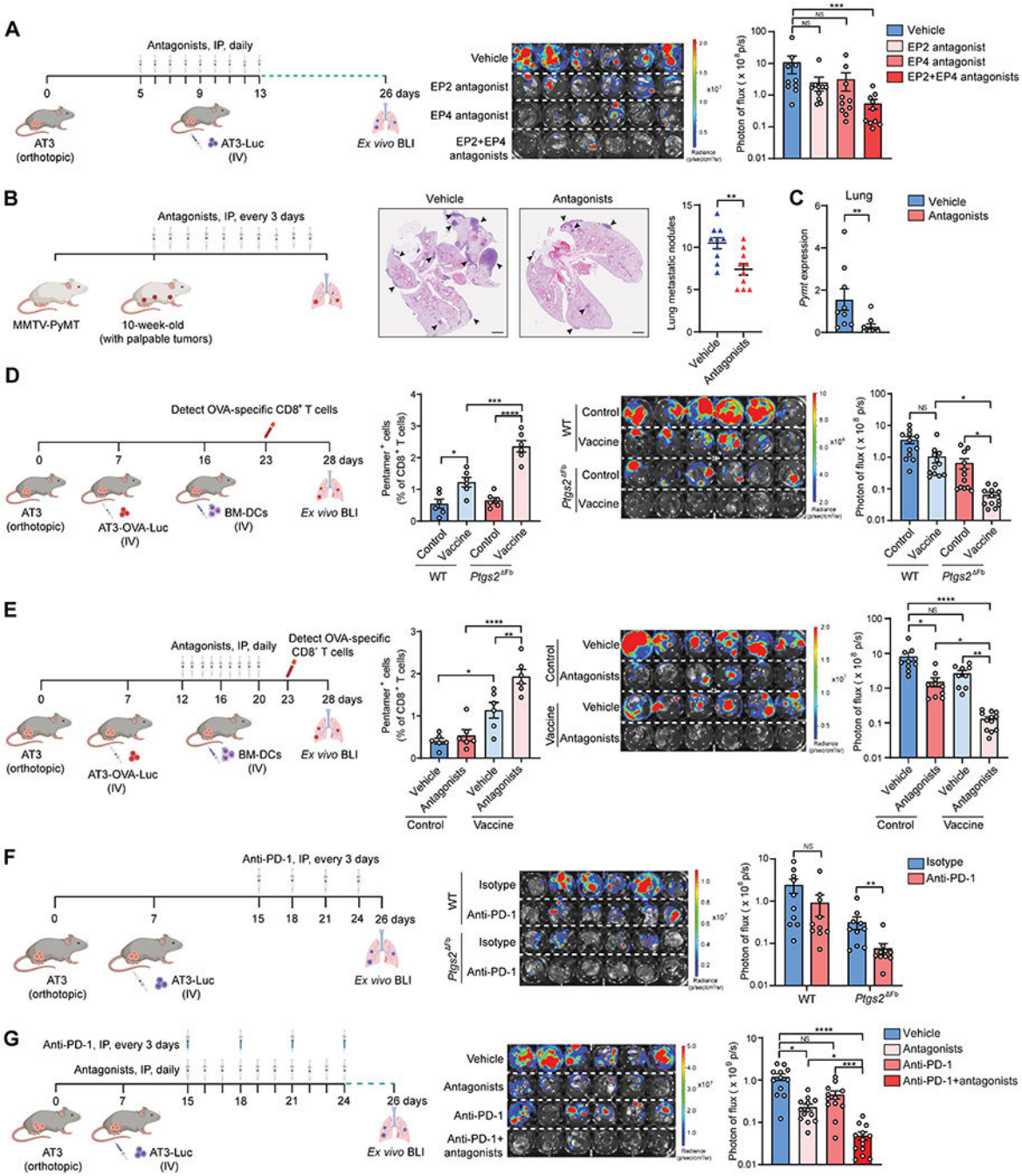

Figure 7. Targeting COX-2-PGE2-EP2/EP4 pathway synergizes with DC vaccine or anti-PD-1 immunotherapy in controlling lung metastasis

(**A**) As depicted in the schematic (*left*), the effect of the single inhibition of EP2 or EP4, or dual inhibition of both receptors, in controlling lung metastatic colonization was determined (n=10).

(**B** and **C**) As depicted in the schematic (*left*), the effect of dual inhibition of EP2 and EP4 in controlling spontaneous lung metastases was determined. Representative H&E images of

lung sections are shown, and the number of lung metastatic nodules was counted (**B**) (n=10). Mammary tumor-specific *Pymt* mRNA level in the lungs was quantified (**C**) (n=9).
(**D** and **E**) As depicted in their respective schematic (*left*), the combined effect of DC vaccine with host fibroblast *Ptgs2* ablation (**D**) or dual inhibition of EP2 and EP4 (**E**) in treating lung metastatic colonization was determined. The frequency of OVA-specific $CD8^+$ T cells in the blood was analyzed (*middle*) (n=6), and lung metastatic colonization was determined (*right*) (n=12 for **D**, and n=9-12 for **E**).
(**F** and **G**) As depicted in their respective schematic (*left*), the combined effect of anti-PD-1 with host fibroblast *Ptgs2* ablation (**F**) or dual inhibition of EP2 and EP4 (**G**) in treating lung metastatic colonization was determined (*right*) (n=10 for **F**, and n=12-13 for **G**).
n is the number of biological replicates. Data are representative of at least three (**A-C, F-G**) or two (**D-E**) independent experiments and shown as mean ± SEM. *p< 0.05, **p< 0.01, ***p< 0.001; ****p< 0.0001; NS, not significant, by Mann-Whitney test (**B-C**, **F**) or one-way ANOVA (**A**, **D-E**, **G**). See also Figure S7.

Key resources table

REAGENT or RESOURCE	SOURCE	IDENTIFIER
Antibodies		
Alexa Fluor® 700 anti-mouse CD45 (Clone 30-F11)	BioLegend	Cat#103128; RRID: AB_493715
APC anti-mouse CD45 (Clone QA17A26)	BioLegend	Cat#157605; RRID: AB_2876537
APC/Fire™ 750 anti-mouse CD45.1 (Clone A20)	BioLegend	Cat#110752; RRID: AB_2629806
PE anti-mouse/human CD11b (Clone M1/70)	BioLegend	Cat#101207; RRID: AB_312790
Brilliant Violet 650™ anti-mouse/human CD11b (Clone M1/70)	BioLegend	Cat#101259; RRID: AB_2566568
PerCP/Cyanine5.5 anti-mouse CD11c (Clone N418)	BioLegend	Cat#117328; RRID: AB_2129641
PE anti-mouse CD11c (Clone N418)	BioLegend	Cat#117307; RRID: AB_313776
APC anti-mouse CD172a (Clone P84)	BioLegend	Cat#144013; RRID: AB_2564060
Anti-mouse/rat XCR1 (Clone QA20A05)	BioLegend	Cat#109402; RRID: AB_2910282
Anti-mouse Ly-6C (Clone HK1.4)	BioLegend	Cat#128001; RRID: AB_1134213
Anti-mouse Ly-6G (Clone 1A8)	BioLegend	Cat#127601; RRID: AB_1089179
Brilliant Violet 570™ anti-mouse Ly-6C (Clone HK1.4)	BioLegend	Cat#128030; RRID: AB_2562617
Pacific Blue™ anti-mouse Ly-6G (Clone 1A8)	BioLegend	Cat#127612; RRID: AB_2251161
PE/Cyanine7 anti-mouse CD24 (Clone M1/69)	BioLegend	Cat#101822; RRID: AB_756048
PE anti-mouse H-2K^{d} (Clone SF1-1.1)	BioLegend	Cat#116607; RRID: AB_313742
PE anti-mouse H-2K^{b}/H-2D^{b} (Clone 28-8-6)	BioLegend	Cat#114607; RRID: AB_313598
APC/Cyanine7 anti-mouse I-A/I-E (Clone M5/114.15.2)	BioLegend	Cat#107627; RRID: AB_1659252
Alexa Fluor® 647 anti-mouse CD19 (Clone 6D5)	BioLegend	Cat#115522; RRID: AB_389329
Alexa Fluor® 647 anti-mouse CD90.2 (Clone 30-H12)	BioLegend	Cat#105318; RRID: AB_492888
Alexa Fluor® 647 anti-mouse Ly-6G (Clone 1A8)	BioLegend	Cat#127610; RRID: AB_1134159
Alexa Fluor® 647 anti-Mouse Siglec-F (Clone E50-2440)	BD Biosciences	Cat#562680; RRID: AB_2687570
APC anti-mouse CD3 (Clone 17A2)	BioLegend	Cat#100236; RRID: AB_2561456
PE/Cyanine5 anti-mouse CD4 (Clone RM4-5)	BioLegend	Cat#100514; RRID: AB_312717
Brilliant Violet 650™ anti-mouse CD8a (Clone 53-6.7)	BioLegend	Cat#100742; RRID: AB_2563056
PE/Cyanine7 anti-mouse CD31 (Clone 390)	BioLegend	Cat#102418; RRID: AB_830757
APC/Fire™ 750 anti-mouse CD326 (Clone G8.8)	BioLegend	Cat#118229; RRID: AB_2629757
Brilliant Violet 421™ anti-mouse CD140a (Clone APA5)	BioLegend	Cat#135923; RRID: AB_2814036
COX-2 antibody (Rabbit)	Cayman Chemical	Cat#160126
GAPDH antibody (Rabbit)	Cell Signaling Technology	Cat#5174S
Goat anti-Rabbit IgG (H+L) Secondary Antibody, HRP	Thermo Fisher Scientific	Cat#31460
Donkey anti-Rabbit IgG (H+L) Highly Cross-Adsorbed Secondary Antibody, Alexa Fluor™ 594. RRID: AB_141637	Thermo Fisher Scientific	Cat#A-21207
Donkey anti-Rabbit IgG (H+L) Highly Cross-Adsorbed Secondary Antibody, Alexa Fluor™ Plus 405	Thermo Fisher Scientific	Cat#A48258
Donkey anti-Rat IgG (H+L) Highly Cross-Adsorbed Secondary Antibody, Alexa Fluor™ Plus 647	Thermo Fisher Scientific	Cat#A48272
Anti-mouse CD3e (Clone 145-2C11)	Bio X Cell	Cat#BE0001-1

REAGENT or RESOURCE	SOURCE	IDENTIFIER
Anti-mouse CD28 (Clone 37.51)	Bio X Cell	Cat#BE0015-1
Anti-mouse PD-1 (Clone RMP1-14)	Bio X Cell	Cat#BE0146
Rat IgG2a isotype control (Clone 2A3)	Bio X Cell	Cat#BE0089
Anti-mouse IL-1β (Clone B122)	Bio X Cell	Cat#BE0246
APC Pro5® MHC Class I Pentamers	ProImmune	Cat#F093-4A-D
Bacterial and virus strains		
Biological samples		
Chemicals, peptides, and recombinant proteins		
Collagenase, Type IV, powder	Thermo Fisher Scientific	Cat#17104019
Dnase I	MilliporeSigma	Cat#DN25
Recombinant Murine IL-4	PeproTech	Cat#214-14
Recombinant Murine GM-CSF	PeproTech	Cat#315-03
Recombinant Murine IL-1β	PeproTech	Cat#211-11B
Ovalbumin, Alexa Fluor™ 647 Conjugate	Thermo Fisher Scientific	Cat#O34784
Prostaglandin E2	Cayman Chemical	Cat#14010
MLN120B	Cayman Chemical	Cat#32819
Celecoxib	Cayman Chemical	Cat#10008672
PF-04418948	Cayman Chemical	Cat#15016
MF498	Cayman Chemical	Cat#15973
D-Luciferin Firefly, potassium salt	Gold Biotechnology	Cat#LUCK
Recombinant Human IL-1β	InvivoGen	Cat#rcyec-hil1b
OVA 257-264	InvivoGen	Cat#vac-sin
OVA 323-339	InvivoGen	Cat#vac-isq
Standard Macrophage Depletion Kit (Clodrosome® + Encapsome®)	Encapsula NanoSciences	Cat#SKU# CLD-8901
Critical commercial assays		
Prostaglandin E2 Parameter Assay Kit	R&D Systems	Cat#KGE004B
Mouse IL-1 beta/IL-1F2 Quantikine ELISA Kit	R&D Systems	Cat#MLB00C
Direct-zol RNA Miniprep Plus w/ TRI Reagent	Zymo	Cat#R2073
High-Capacity cDNA Reverse Transcription Kit	Thermo Fisher Scientific	Cat#4368814
PowerUp SYBR™ Green PCR Master Mix	Thermo Fisher Scientific	Cat#A25778
Dynabeads Mouse T-Activator CD3/28	Thermo Fisher Scientific	Cat#11-456-D
CellTrace™ CFSE Cell Proliferation Kit	Thermo Fisher Scientific	Cat#C34554
CellTracker™ Orange CMTMR Dye	Thermo Fisher Scientific	Cat#C2927
CellTracker™ Deep Red Dye	Thermo Fisher Scientific	Cat#C34565

REAGENT or RESOURCE	SOURCE	IDENTIFIER
Cytofix/Cytoperm kit	BD Biosciences	Cat#555028
Precision Count Beads	Biolegend	Cat#424902
CD4 (L3T4) Microbeads	Miltenyi Biotec	Cat#130-117-043
CD8a (Ly-2) Microbeads	Miltenyi Biotec	Cat#130-117-044
CD90.2 Microbeads	Miltenyi Biotec	Cat#130-121-278
NK Cell Isolation Kit	Miltenyi Biotec	Cat#130-115-818
Monocyte Isolation Kit (BM)	Miltenyi Biotec	Cat#130-100-629
Anti-Ly6G MicroBeads	Miltenyi Biotec	Cat#130-120-337
Deposited data		
RNA-seq data of BM-DCs	This paper	ArrayExpress: E-MTAB-11873
RNA-seq data of lung myeloid cells from WT and *Ptgs2*-cKO mice	This paper	ArrayExpress: E-MTAB-11888
RNA-seq data of *ex vivo* cultured lung fibroblasts	This paper	ArrayExpress: E-MTAB-11887
scRNA-seq data of lung stromal cells	This paper	ArrayExpress: E-MTAB-11879
scRNA-seq data of lung CD140a^{+} fibroblasts	This paper	ArrayExpress: E-MTAB-11875
scRNA-seq data of lung immune cells from WT and *Ptgs2*-cKO mice	This paper	GEO: GSE206449
scRNA-seq data of human idiopathic pulmonary fibrosis samples	(Habermann et al., 2020)	GEO: GSE135893
scRNA-seq data of hfuman lung tissues	(Travaglini et al., 2020)	EGA: EGAS00001004344
Microarray datasets of human normal tissues	(Roth et al., 2006)	GEO: GSE7307, GSE3526
Experimental models: Cell lines		
4T1	ATCC	Cat#CRL-2539
AT3	Gift from S.I. Abrams	N/A
E0771	CH3 Biosystems	Cat#940001
YAC-1	ATCC	Cat#TIB-160
4T1-Luc	(Li et al., 2020a)	N/A
4T1-GFP	This paper	N/A
AT3-*gcsf*	(Gong et al., 2022)	N/A
AT3-Luc	(Li et al., 2020a)	N/A
AT3-mCherry	(Li et al., 2020a)	N/A
AT3-GFP	(Li et al., 2020b)	N/A
AT3-*gcsf*-GFP	This paper	N/A
AT3-OVA-Luc	This paper	N/A
E0771-Luc	(Li et al., 2020a)	N/A
E0771-GFP	This paper	N/A
Human lung mesenchymal cells	Sciencell	Cat#7540
Experimental models: Organisms/strains		
BALB/cJ	The Jackson Laboratory	JAX: 000651
C57BL/6J	The Jackson Laboratory	JAX: 000664
OT-I: C57BL/6-Tg(TcraTcrb)1100Mjb/J	The Jackson Laboratory	JAX: 003831
OT-II: B6.Cg-Tg(TcraTcrb)425Cbn/J	The Jackson Laboratory	JAX: 004194

REAGENT or RESOURCE	SOURCE	IDENTIFIER
Ptgs2$^{-/-}$: B6;129S-*Ptgs2*^{tm1Jed}/J	The Jackson Laboratory	JAX: 002476
Ptgs2^{Luc}: B6;129S4-*Ptgs2*$^{tm2.1Hahe}$/J	The Jackson Laboratory	JAX: 030853
Ptgs2$^{flox/flox}$: B6;129S4-*Ptgs2*^{tm1Hahe}/J	The Jackson Laboratory	JAX: 030785
Pdgfra^{Cre}: C57BL/6-Tg(*Pdgfra*-cre)1Clc/J	The Jackson Laboratory	JAX: 013148
Pdgfra^{Cre}; *Ptgs2*$^{flox/flox}$	This paper	N/A
FVB/N-Tg(MMTV-PyVT)634Mul/J	The Jackson Laboratory	JAX: 002374
MMTV-PyMT: B6.FVB-Tg(MMTV-PyVT)634Mul/LellJ	The Jackson Laboratory	JAX: 022974
B6 Cd45.1 (B6.SJL-*Ptprc*^{a} *Pepc*^{b}/BoyJ)	The Jackson Laboratory	JAX: 002014
Pdgfa^{Cre}; *Ptgs2*$^{flox/flox}$; MMTV	This paper	N/A
Il1r1$^{-/-}$: B6.129S7-*Il1r1*^{tm1Imx}/J	The Jackson Laboratory	JAX: 003245
CD140a^{EGFP}: B6.129S4-*Pdgfra*$^{tm11(EGFP)Sor}$/J	The Jackson Laboratory	JAX: 007669
Oligonucleotides		
See Table S1 for primer sequences		
Recombinant DNA		
pLenti CMV Puro LUC (w168-1)	(Campeau et al., 2009)	Addgene#17477
pLV-mCherry	Tsoulfas lab	Addgene #36084
pcDNA3-OVA	(Diebold et al., 2001)	Addgene #64599
Software and algorithms		
BD FACSDiva software	BD Biosciences	https://www.bdbiosciences.com/
FlowJo	BD Biosciences	https://flowjo.com
R (version 4.0.2)	R Core Team (2020)	https://www.r-project.org/
Seurat (version 3.2.2)	Satija Lab	https://satijalab.org/seurat/
limma (version 3.46.0)	(Ritchie et al., 2015)	https://bioconductor.org/packages/release/bioc/html/limma.html
Metascape	(Zhou et al., 2019)	https://metascape.org/
DoRothEA (version 1.1.2)	(Holland et al., 2020)	https://saezlab.github.io/dorothea/
Ingenuity Pathway Analysis	QIAGEN	https://www.qiagenbioinformatics.com/products/ingenuity-pathway-analysis/
GraphPad Prism (version 8.2.1)	GraphPad Software	https://www.graphpad.com/
Biorender	Biorender	https://biorender.com/
ImageJ (1.53c)	ImageJ	https://imagej.nih.gov/ij/
Other		